LOFAR low-band antenna observations of the 3C295 and Bootes fields: source counts and ultra-steep spectrum sources

R. J. van Weeren, W. L. Williams, C. Tasse, H. J. A. Rottgering, D. A. Rafferty, S. van Der Tol, G. Heald, G. J. White, A. Shulevski, P. Best, et al.

The Astrophysical Journal, 793:82 (22pp), 2014 October 1 doi:10.1088/0004-637X/793/2/82

LOFAR LOW-BAND ANTENNA OBSERVATIONS OF THE 3C 295 AND BOÖTES FIELDS: SOURCE COUNTS AND ULTRA-STEEP SPECTRUM SOURCES

R. J. van Weeren[1,50], W. L. Williams[2,3], C. Tasse[4,5,6], H. J. A. Röttgering[2], D. A. Rafferty[2], S. van der Tol[2,3], G. Heald[3], G. J. White[7,8], A. Shulevski[9], P. Best[10], H. T. Intema[11], S. Bhatnagar[11], W. Reich[12], M. Steinmetz[13], S. van Velzen[14], T. A. Enßlin[15], I. Prandoni[16], F. de Gasperin[17], M. Jamrozy[18], G. Brunetti[16], M. J. Jarvis[19,20,21], J. P. McKean[3,9], M. W. Wise[3,22], C. Ferrari[23], J. Harwood[24], J. B. R. Oonk[3], M. Hoeft[25], M. Kunert-Bajraszewska[26], C. Horellou[27], O. Wucknitz[12], A. Bonafede[17], N. R. Mohan[28], A. M. M. Scaife[29], H.-R. Klöckner[12], I. M. van Bemmel[3], A. Merloni[30], K. T. Chyzy[18], D. Engels[17], H. Falcke[3,12,14], M. Pandey-Pommier[31,32,33], A. Alexov[34], J. Anderson[13], I. M. Avruch[3,35], R. Beck[12], M. E. Bell[36], M. J. Bentum[3,37], G. Bernardi[1], F. Breitling[13], J. Broderick[29], W. N. Brouw[3,9], M. Brüggen[17], H. R. Butcher[38], B. Ciardi[15], E. de Geus[3,39], M. de Vos[3], A. Deller[3], S. Duscha[3], J. Eislöffel[25], R. A. Fallows[3], W. Frieswijk[3], M. A. Garrett[2,3], J. Grießmeier[40,41], A. W. Gunst[3], J. P. Hamaker[3], T. E. Hassall[29,42], J. Hörandel[14], A. van der Horst[22], M. Iacobelli[2], N. J. Jackson[42], E. Juette[43], V. I. Kondratiev[3,44], M. Kuniyoshi[12], P. Maat[3], G. Mann[13], D. McKay-Bukowski[45,46], M. Mevius[3,9], R. Morganti[3,9], H. Munk[3], A. R. Offringa[38], E. Orrù[3], H. Paas[47], V. N. Pandey[3], G. Pietka[19], R. Pizzo[3], A. G. Polatidis[3], A. Renting[3], A. Rowlinson[22], D. Schwarz[48], M. Serylak[19], J. Sluman[3], O. Smirnov[4,5], B. W. Stappers[42], A. Stewart[28], J. Swinbank[22], M. Tagger[40], Y. Tang[3], S. Thoudam[14], C. Toribio[3], R. Vermeulen[3], C. Vocks[13], and P. Zarka[49]

[1] Harvard-Smithsonian Center for Astrophysics, 60 Garden Street, Cambridge, MA 02138, USA; rvanweeren@cfa.harvard.edu
[2] Leiden Observatory, Leiden University, P.O. Box 9513, NL-2300 RA Leiden, The Netherlands
[3] Netherlands Institute for Radio Astronomy (ASTRON), P.O. Box 2, NL-7990 AA Dwingeloo, The Netherlands
[4] Department of Physics and Electronics, Rhodes University, P.O. Box 94, Grahamstown 6140, South Africa
[5] SKA South Africa, 3rd Floor, The Park, Park Road, Pinelands 7405, South Africa
[6] GEPI, Observatoire de Paris, CNRS, Université Paris Diderot, 5 place Jules Janssen, F-92190 Meudon, France
[7] Department of Physics and Astronomy, The Open University, Buckinghamshire MK7 6AA, UK
[8] Space Science Department, Rutherford Appleton Laboratory, Chilton, Oxfordshire OX11 0QX, UK
[9] Kapteyn Astronomical Institute, P.O. Box 800, NL-9700 AV Groningen, The Netherlands
[10] Institute for Astronomy, University of Edinburgh, Royal Observatory of Edinburgh, Blackford Hill, Edinburgh EH9 3HJ, UK
[11] National Radio Astronomy Observatory, Socorro, NM 87801, USA
[12] Max-Planck-Institut für Radioastronomie, Auf dem Hügel 69, D-53121 Bonn, Germany
[13] Leibniz-Institut für Astrophysik Potsdam (AIP), An der Sternwarte 16, D-14482 Potsdam, Germany
[14] Department of Astrophysics, Institute for Mathematics, Astrophysics and Particle Physics (IMAPP), Radboud University Nijmegen, P.O. Box 9010, NL-6500 GL Nijmegen, The Netherlands
[15] Max Planck Institute for Astrophysics, Karl-Schwarzschildstrasse 1, D-85748 Garching, Germany
[16] INAF—Istituto di Radioastronomia, Via Gobetti 101, I-40129 Bologna, Italy
[17] Hamburger Sternwarte, University of Hamburg, Gojenbergsweg 112, D-21029 Hamburg, Germany
[18] Astronomical Observatory, Jagiellonian University, ul. Orla 171, 30-244 Kraków, Poland
[19] Astrophysics, Department of Physics, Keble Road, Oxford OX1 3RH, UK
[20] Centre for Astrophysics, Science and Technology Research Institute, University of Hertfordshire, Hatfield, Hertfordshire AL10 9AB, UK
[21] Physics Department, University of the Western Cape, Private Bag X17, Bellville 7535, South Africa
[22] Astronomical Institute "Anton Pannekoek," University of Amsterdam, Postbus 94249, NL-1090 GE Amsterdam, The Netherlands
[23] Laboratoire Lagrange, UMR7293, Université de Nice Sophia-Antipolis, CNRS, Observatoire de la Côte d'Azur, F-06300 Nice, France
[24] School of Physics, Astronomy and Mathematics, University of Hertfordshire, College Lane, Hatfield, Hertfordshire AL10 9AB, UK
[25] Thüringer Landessternwarte, Sternwarte 5, D-07778 Tautenburg, Germany
[26] Toruń Centre for Astronomy, Faculty of Physics, Astronomy and Informatics, NCU, Grudziacka 5, 87-100 Toruń, Poland
[27] Department of Earth and Space Sciences, Chalmers University of Technology, Onsala Space Observatory, SE-43992 Onsala, Sweden
[28] National Centre for Radio Astrophysics, TIFR, Pune University Campus, Post Bag 3, Pune 411007, India
[29] School of Physics and Astronomy, University of Southampton, Highfield, Southampton SO17 1BJ, UK
[30] Max-Planck Institut für Extraterrestrische Physik, Giessenbachstrasse, D-85748 Garching, Germany
[31] Université de Lyon, F-69003 Lyon, France
[32] Centre de Recherche Astrophysique de Lyon, Observatoire de Lyon, 9 av Charles André, F-69561 Saint Genis Laval Cedex, France
[33] Ecole Normale Supérieure de Lyon, F-69007 Lyon, France
[34] Space Telescope Science Institute, 3700 San Martin Drive, Baltimore, MD 21218, USA
[35] SRON Netherlands Institute for Space Research, P.O. Box 800, NL-9700 AV Groningen, The Netherlands
[36] ARC Centre of Excellence for All-sky astrophysics (CAASTRO), Sydney Institute of Astronomy, University of Sydney Australia, NSW 2006, Australia
[37] University of Twente, Postbus 217, 7500-AE Enschede, The Netherlands
[38] Research School of Astronomy and Astrophysics, Australian National University, Mt Stromlo Obs., via Cotter Road, Weston, ACT 2611, Australia
[39] SmarterVision BV, Oostersingel 5, NL-9401 JX Assen, The Netherlands
[40] LPC2E—Universite d'Orleans/CNRS, F-45067 Orléans Cédex 2, France
[41] Station de Radioastronomie de Nancay, Observatoire de Paris—CNRS/INSU, USR 704—Universite d'Orleans, OSUC, Route de Souesmes, F-18330 Nancay, France
[42] Jodrell Bank Center for Astrophysics, School of Physics and Astronomy, The University of Manchester, Manchester M13 9PL, UK
[43] Astronomisches Institut der Ruhr-Universität Bochum, Universitaetsstrasse 150, D-44780 Bochum, Germany
[44] Astro Space Center of the Lebedev Physical Institute, Profsoyuznaya Str. 84/32, Moscow 117997, Russia
[45] Sodankylä Geophysical Observatory, University of Oulu, Tähteläntie 62, FI-99600 Sodankylä, Finland
[46] STFC Rutherford Appleton Laboratory, Harwell Science and Innovation Campus, Didcot OX11 0QX, UK
[47] Center for Information Technology (CIT), University of Groningen, NL-9712 CP Groningen, The Netherlands
[48] Fakultät für Physik, Universität Bielefeld, Postfach 100131, D-33501 Bielefeld, Germany
[49] LESIA, UMR CNRS 8109, Observatoire de Paris, F-92195 Meudon, France

Received 2014 April 24; accepted 2014 July 26; published 2014 September 9

ABSTRACT

We present Low Frequency Array (LOFAR) Low Band observations of the Boötes and 3C 295 fields. Our images made at 34, 46, and 62 MHz reach noise levels of 12, 8, and 5 mJy beam^{-1}, making them the deepest images ever obtained in this frequency range. In total, we detect between 300 and 400 sources in each of these images, covering an area of 17–52 deg^2. From the observations, we derive Euclidean-normalized differential source counts. The 62 MHz source counts agree with previous GMRT 153 MHz and Very Large Array 74 MHz differential source counts, scaling with a spectral index of −0.7. We find that a spectral index scaling of −0.5 is required to match up the LOFAR 34 MHz source counts. This result is also in agreement with source counts from the 38 MHz 8C survey, indicating that the average spectral index of radio sources flattens toward lower frequencies. We also find evidence for spectral flattening using the individual flux measurements of sources between 34 and 1400 MHz and by calculating the spectral index averaged over the source population. To select ultra-steep spectrum ($\alpha < -1.1$) radio sources that could be associated with massive high-redshift radio galaxies, we compute spectral indices between 62 MHz, 153 MHz, and 1.4 GHz for sources in the Boötes field. We cross-correlate these radio sources with optical and infrared catalogs and fit the spectral energy distribution to obtain photometric redshifts. We find that most of these ultra-steep spectrum sources are located in the $0.7 \lesssim z \lesssim 2.5$ range.

Key words: galaxies: active – radio continuum: general – surveys – techniques: interferometric

Online-only material: color figures, machine-readable table

1. INTRODUCTION

Low-frequency surveys of the sky are an important tool to address various open questions in astrophysics ranging from the evolution of galaxies, active galactic nuclei (AGNs), and galaxy clusters to pulsars. The half power beam width (HPBW) of radio telescopes scales with wavelength, making low-frequency radio observations ($\lesssim$300 MHz) an efficient way to carry out large-area surveys. In addition, these observations take advantage of the steep synchrotron spectra ($F_\nu \propto \nu^\alpha$, with α the spectral index) of many extragalactic radio sources, with the flux densities increasing toward lower frequencies.

Low-frequency observations are particularly important to locate distant high-redshift radio galaxies (HzRGs). Empirically it has been found that the radio spectral index correlates with the redshift of host galaxies, with the steepest spectra corresponding to the highest redshifts. Therefore massive high-redshift galaxies can be found by selecting radio sources with ultra-steep radio spectra (USS), especially in combination with an optical or near-IR magnitude cut (e.g., De Breuck et al. 2000; Miley & De Breuck 2008; Ker et al. 2012). However, USS sources are rare so large surveys are needed to find them. The fraction of USS sources with $\alpha_{\sim 350}^{1400} < -1.3$ is about 0.5% (De Breuck et al. 2000). Deep observations at $\lesssim$150 MHz have the potential to detect sources with $\alpha \lesssim -2$ because these sources become too faint to be detected in sensitive high-frequency observations.

Radio sources in the last stages of the AGN evolution (both short- and long-lived) are also most efficiently selected at low frequencies. These relic or dying radio sources have steep and curved radio spectra due to synchrotron and inverse Compton losses as the central energy supply has been switched off (e.g., Parma et al. 2007; Kunert-Bajraszewska et al. 2010; Murgia et al. 2011).

Recently, most deep low-frequency surveys have been carried out with the GMRT at around 150 MHz (e.g., Ishwara-Chandra & Marathe 2007; Sirothia et al. 2009; Ishwara-Chandra et al. 2010; Intema et al. 2011; Williams et al. 2013). These surveys reach a rms noise level of the order of a mJy per beam. Below 100 MHz, there are no radio surveys that reach a similar depth. Cohen et al. (2004) carried out a 165 deg^2 74 MHz survey with a central noise of 24 mJy beam^{-1} at a resolution of 25″. Tasse et al. (2006) surveyed the *XMM*-LSS field at 74 MHz with a resolution of 30″, covering an area of 132 deg^2. The median rms noise over the field was 32 mJy beam^{-1}. Larger but shallower surveys below 100 MHz are the 74 MHz VLSS (Cohen et al. 2007; Lane et al. 2012) and 38 MHz (Hales et al. 1995; Rees 1990) surveys.

The Low Frequency Array (LOFAR) is a new generation radio telescope operating at 10–240 MHz (van Haarlem et al. 2013). With its multi-beaming capabilities, high spatial resolution, and large fractional bandwidth, it is an ideal instrument to carry out large surveys. Here we report on the first LOFAR Low Band Antenna (LBA) commissioning observations of the Boötes and the 3C 295 fields (which includes the Groth strip). Both the Boötes field and the Groth strip have been extensively studied at higher radio frequencies and other parts of the electromagnetic spectrum. For the Boötes field, observations have been carried out at 153 MHz (Intema et al. 2011; Williams et al. 2013), 325 MHz (Croft et al. 2008), 1.4 GHz (de Vries et al. 2002; Higdon et al. 2005), and 3.1 GHz (Croft et al. 2013). The Groth strip has been observed at 1.4 GHz (Ivison et al. 2007).

The outline of this paper is as follows. The observations and data reduction are described in Section 2. The results and analysis are presented in Sections 3 and 4. This is followed by the conclusions in Section 5. All coordinates and images use the J2000 coordinate system.

2. OBSERVATIONS AND DATA REDUCTION

The Boötes and 3C 295 fields were simultaneously observed on 2012 April 12 as part of a multi-beam observation with the LOFAR LBA stations. The idea behind the multi-beam setup is that we use the 3C 295 observations as a calibrator field to transfer the gain amplitudes to the (target) Boötes field. The total integration time on both fields was 10.25 hr. An overview of the observations is given in Table 1. Complete frequency coverage was obtained between 54 and 70 MHz for both fields, while non-contiguous frequency coverage was obtained between 30 and 54 MHz for the 3C 295 only. All four correlation products were recorded. By default, the frequency band was divided into sub-bands, each 195.3125 kHz wide. Each sub-band was further divided in 64 channels and the integration time was 1 s.

[50] Einstein Fellow.

Table 1
LBA Observations

Observations ID	L56691
Pointing center 3C 295	$14^h11^m20^s.9$, $+52°13'55''$
Pointing center Boötes	$14^h32^m03^s.0$, $+34°16'33''$
Integration time	1 s
Observation date	2012 Apr 12
Total on-source time	10.25 hr
Correlations	XX, XY, YX, YY
Frequency setup (a)	54–70 MHz full coverage
Frequency setup (b)	40–54 MHz 25 sub-bands*
Frequency setup (c)	30–40 MHz 21 sub-bands*
Bandwidth (a, b, c)	16 MHz, 4.9 MHz, 4.1 MHz
Bandwidth per sub-band	195.3125 kHz
Channels per sub-band	64

Notes. (a) 54–70 MHz Boötes and 3C 295 fields. (b) 40–54 MHz 3C 295 field. (c) 30–44 MHz 3C 295 field. *Sub-bands are more or less evenly distributed within this frequency range, the total bandwidth is reported in Table 2.

Nine Dutch remote stations were used along with 22 core stations, giving baselines that range between 90 m and 80 km. The resulting uv coverage is displayed in Figure 1. The LBA_OUTER configuration was used. In the LBA_OUTER configuration, 48 LBA antennas are used, located mostly in the outer part of the stations (which have diameters of about 81 m). This increases the sidelobe levels for the station beams, but reduces the field of view (FoV) with respect to other station antenna configurations available. The HPBW is about $3.^\circ6$, $4.^\circ8$, and $7.^\circ2$ at 60, 45, and 30 MHz, respectively. It should be noted though that the station beams are complex-valued, time and direction dependent, and differ from station to station.

2.1. Data Reduction

Our data reduction broadly consists of the following steps: (1) flagging, (2) bright off-axis source removal, (3) averaging, (4) solving for the 3C 295 complex gains (in a circular basis to deal with differential Faraday rotation), (5) transfer of the amplitude solutions from 3C 295 to the Boötes field, (6) phase-only calibration of the Boötes field against a GMRT model, and (7) imaging of the 3C 295 field and Boötes fields. All calibration steps are performed with the `BlackBoard Selfcal` (`BBS`) software system (Pandey et al. 2009). Below these steps are explained in more detail.

2.1.1. Flagging, Bright Off-axis Source Removal, and Averaging

The first step in the reduction consisted of the automatic flagging of radio frequency interference (RFI) using the `AOFlagger` (Offringa et al. 2010, 2012). The first and last three channels of each sub-band were also flagged. Typically, about 2% of the data was flagged as RFI in the 50–70 MHz range. Between 30 and 40 MHz this percentage increases by a factor of approximately two to three (see Offringa et al. 2013, for an overview of the LOFAR RFI environment). About a dozen sub-bands were lost due to failures of the data storage system.

A next step consisted of the removal of the bright "A-team" radio sources Cas A and Cyg A. These sources have integrated flux densities of 18 and 17 kJy at 74 MHz, respectively. Although they are located outside the main FoV, they are sufficiently bright to prevent proper calibration and imaging of sources in the central part of the FoV if detected in the secondary lobes of the beam. The amplitudes of these off-axis sources are strongly modulated as they move in and out of the station beam sidelobes. These sources were removed with the "demixing" method described by van der Tol et al. (2007), which is part of the standard LOFAR pre-processing pipeline (Heald et al. 2010). For the models of Cas A and Cyg A, we took the clean component models at 74 MHz from Very Large Array (VLA) A-array[51] observations (Kassim et al. 2007) with a resolution of $25''$. After flagging and subtracting out Cas A and Cyg A, we averaged the data in time to 5 s and one channel per sub-band. The time resolution is set by the requirement to avoid decorrelation due to rapid ionospheric phase variations. At large radial distances from the field center there is some bandwidth smearing. At the HPBW, the source width increases by a factor of ∼1.2 at 62 MHz and a factor of ∼1.9 at 34 MHz, due to this effect.

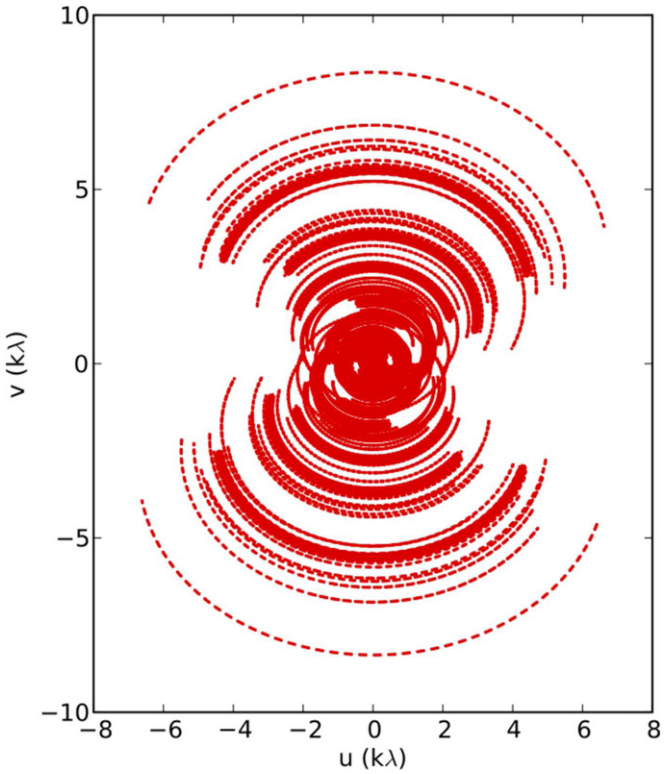

Figure 1. UV coverage of the 3C 295 observations. The relatively large fractional bandwidth fills the uv plane radially (not shown in the figure).
(A color version of this figure is available in the online journal.)

2.1.2. 3C 295 Field

The primary calibrator 3C 295 has a sufficiently high flux density that it dominates the total flux in the main FoV. 3C 295 consists of two main source components (e.g., Perley & Taylor 1991) and has an angular size of only $\sim5''$. Given that our longest baseline is ∼80 km (corresponding to a resolution of about $10''$), we used a simple two clean component model for the source. The integrated flux density of the source is given by the model of Scaife & Heald (2012).

Before calibrating, we converted the linear XX, XY, YX, YY correlations (V_{XY}) to circular RR, RL, LR, LL correlations V_{RL} using the transformation described by Hamaker & Bregman (1996):

$$V_{RL} = C_A V_{XY} C_A^*, \quad (1)$$

[51] http://lwa.nrl.navy.mil/tutorial/

with

$$C_A = \frac{1}{\sqrt{2}} \begin{pmatrix} 1 & i \\ 1 & -i \end{pmatrix}. \quad (2)$$

This transformation was done via a Python script. The effects of the station beams[52] were taken out as well in the direction of 3C 295 with BBS. This is needed because the LBA stations do not record "true" linear correlation products due to the fixed orientation of the dipole antennas on the ground.

The (only) reason for converting to circular correlations is that differential Faraday rotation, which is important in the LBA frequency range, only affects the RR and LL phases, while in linear correlations, flux from XX and YY leaks into the cross-hand XY and YX correlations. Therefore by converting to circular correlations the calibration is simplified, since we only have to solve for the RR and LL phases to remove the effects of differential Faraday rotation (e.g., Smirnov 2011). The conversion from linear to circular correlations depends on the accuracy of the beam models. It is also possible to solve for differential Faraday rotation in a more direct way using the observed linear correlations but this requires solving for an extra free parameter.

After converting to circular correlations we obtained amplitude and phase solutions for the RR and LL correlations for each sub-band using the 3C 295 model (with BBS). We used a solution interval of 5 s. This takes care of the frequency dependence of ionospheric phase variations, differential Faraday rotation, clock errors, and the overall LBA bandpass (with a single complex gain correction for each time interval per sub-band). Good quality solutions were obtained over the entire time and frequency range, except for time periods affected by RFI. We then subtracted 3C 295 from the data using these gain solutions. This avoids many clean cycles and clean dynamic range limitations such as described in Cotton & Uson (2008). After the 3C 295 gain calibration, we converted back the calibrated visibilities from circular to linear correlations because of limitations in the imaging software.

2.1.3. Boötes Field

We transferred the amplitude solutions from the corresponding frequencies of the 3C 295 observation to the Boötes field data set. The Boötes field does not contain any bright dominating sources. This means that there is not enough signal available per sub-band for a phase-only calibration on a timescale of 5 s. To increase the signal to noise, all sub-bands were combined into a new measurement set consisting of 81 channels covering the entire 54–70 MHz range, with each channel corresponding to one individual sub-band. We then performed a phase-only calibration for groups of 27 channels each to obtain sufficient signal to noise to calibrate the distant remote stations against the GMRT 153 MHz model.

For the Boötes field, the calibration model is derived from a deep GMRT 153 MHz image (Williams et al. 2013) using the PyBDSM source detection software.[53]

2.2. Imaging and Cleaning

Imaging and cleaning was carried out with awimager (Tasse et al. 2013), which incorporates the complex valued, time varying and frequency dependent individual station beams using A-Projection (Bhatnagar et al. 2008). For LOFAR, all 4×4 Mueller terms have to be taken into account in the A-Projection. For awimager, a hybrid AW-projection algorithm was developed to apply the time, frequency, baseline, and direction dependent effects in full-polarization in an efficient way. Also, a new parallel gridding technique is used, which differs from the casapy[54] gridder.

For the imaging, we combined all available 54–70 MHz sub-bands for the Boötes and 3C 295 fields to improve the uv coverage with multi-frequency synthesis. We did not correct for the spectral index of individual sources (Rau & Cornwell 2011) because such an algorithm is not yet implemented for awimager. For the 3C 295 field, we made two additional images from the sub-bands in the ranges 30–40 MHz and 40–54 MHz. We employed various robust weighting schemes (Briggs 1995) to find that a robust parameter of about 0.0 typically gave the lowest rms noise level. All final images have sizes of 8192^2 pixels and were made with a robust value of 0.0 and all baselines were included. The point-spread functions for the 54–70 MHz images are shown in Figure 2. An overview of the image properties is given in Table 2.

We used clean masks during the final imaging step to minimize clean bias effects (e.g., Condon et al. 1998; White et al. 1997). The mask was derived from a previous imaging run without any mask. The clean mask was generated with PyBDSM, detecting islands of emission with a $3\sigma_{\rm rms}$ island threshold, a pixel threshold of $5\sigma_{\rm rms}$, and a locally varying rms box with a size of 80×80 pixels to take into account artifacts around strong sources. The 80 pixels approximately correspond to the spatial scale over which the local rms noise changes in the presence of strong sources. Maps of the local rms noise are shown in Figure 3.

3. RESULTS

An overview of the resulting images, resolution, FoV, and noise levels obtained is given Table 2. The primary beam corrected images are displayed in Figures 4–7. The artifacts visible around the brighter sources in the fields are due to imperfect calibration and errors in the station beam model. These artifacts also give rise to the increased noise around bright sources (Figure 3). The "spoke"-like patterns are likely caused by direction dependent ionospheric phase errors. The spokes are not visible at the position of 3C 295 because the ionospheric phase variations in this direction were properly taken into account (phase calibration was performed in the 3C 295 direction).

The "smudge" visible in the 3C 295 field (labeled with a circle in Figures 6 and 7) at $14^{\rm h}03^{\rm m}$ $+54^{\circ}21'$ is the galaxy NGC 5457 (M101). In the Boötes field, faint diffuse emission is found at $14^{\rm h}21\overset{\rm m}{.}5$ $+35^{\circ}12'$, labeled with a circle in Figure 4. This source (1421+35) was previously also noted by Delain & Rudnick (2006) and Williams et al. (2013). A more detailed study of the source was performed by de Gasperin et al. (2014). They conclude that the extended radio emission is the remnant of a past AGN activity cycle of NGC 5590 at $z = 0.0107$.

3.1. Source Detection

We used the PyBDSM software for source detection. PyBDSM works by identifying islands of contiguous pixels above a certain

[52] The station beam model is derived using the dipole beam model based on the interpolation of electromagnetic simulations of the LBA dipole beam response and the dipole locations within a station (Hamaker 2011).

[53] http://dl.dropboxusercontent.com/u/1948170/html/index.html

[54] http://casa.nrao.edu

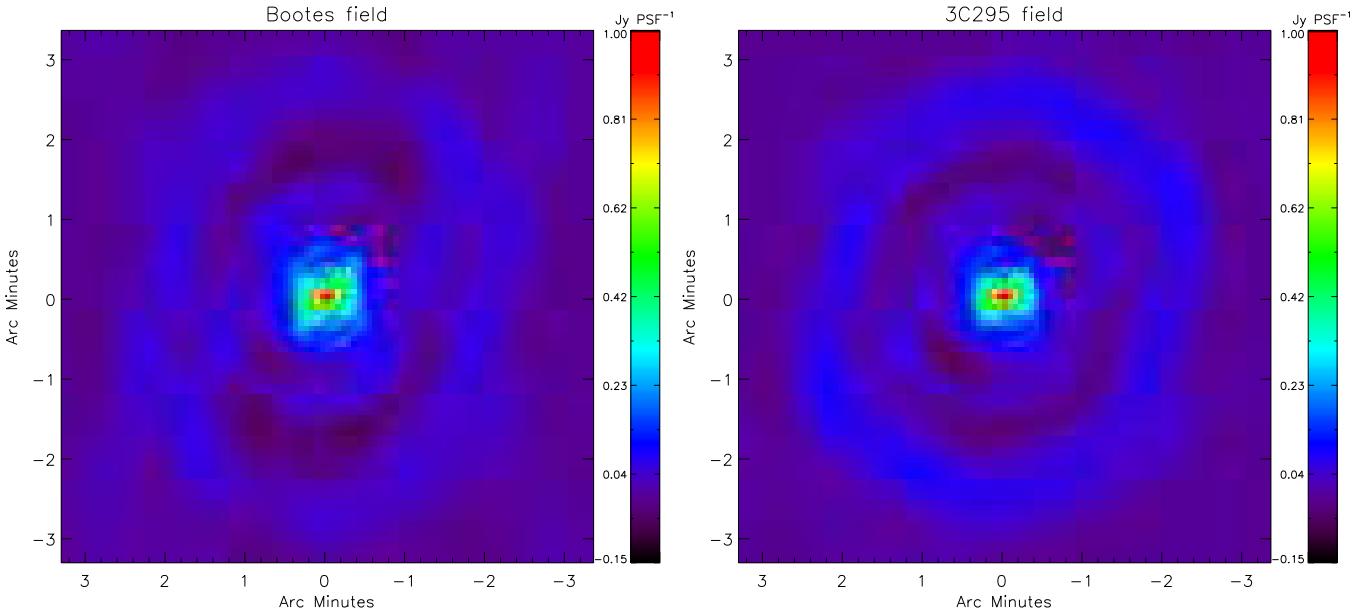

Figure 2. Point-spread functions for the Boötes (left) and 3C 295 (right) images covering the 54–70 MHz frequency range.
(A color version of this figure is available in the online journal.)

Table 2
LOFAR LBA Image Characteristics

Field	Frequency (MHz)	Field of View[a] (deg^2)	Bandwidth (MHz)	rms Noise ($\sigma_{\rm rms}$) (mJy beam^{-1})	Synthesized Beam (arcsec)	Pixel Size (arcsec)
Boötes	62	19.4	16	4.8	31 × 19	4.0
3C 295	62	17.0	16	5.3	29 × 18	4.0
3C 295	46	30.5	4.9	8.2	40 × 24	6.0
3C 295	34	52.3	4.1	12	56 × 30	8.0

Note. [a] With a primary beam correction factor <0.4.

detection threshold and fitting each island with Gaussians. For detecting islands, we took a threshold of $3\sigma_{\rm rms}$ and a pixel threshold of $5\sigma_{\rm rms}$, meaning that at least one pixel in each island needs to be above $5\sigma_{\rm rms}$. We used a locally varying rms noise with a sliding box size of 80 × 80 pixels to take into account the rms noise increase around the bright sources. We manually inspected the output source catalogs to remove about a dozen false detections. These false detections were associated to sidelobes near bright sources. No sources beyond a primary beam attenuation factor of 0.4 were included.

Because the sources are distorted and smeared and this distortion varies across FoV due to the ionosphere, the fitted major and minor axes for the Gaussian components cannot be simply used to determine whether a source is resolved or not. To first order, the derived integrated flux densities for the sources should not be affected by the smearing. We carried out a visual inspection for actual resolved sources, images of these sources are given in Appendix A. In Figure 8, we plot histograms of the fitted major and minor axes for the sources in the 3C 295 and Boötes fields. The decrease of the effective resolution toward lower frequencies can be seen by the broadening of the distribution of fitted major and minor axes. The final source list at 62 MHz contains 329 sources for both the Boötes and 3C 295 fields. At 46 and 34 MHz, the lists contain 367 and 392 sources for the 3C 295 field, respectively. Our LBA images reach a similar depth as the 325 MHz WENSS survey (scaling with a spectral index of −0.7). Because of the ionospheric distortions, we do not classify resolved or unresolved sources. The uncertainties for the measured flux densities and positions are discussed in Sections 3.2 and 3.3. An example of the source catalogs is shown in Table 3. For each source, we list the source name, the flux-weighted coordinates and uncertainties, and the integrated flux densities and uncertainties.

3.2. Astrometric Uncertainties

Ionospheric phase distortions and residual calibration errors can have an effect on the source positions. To assess the accuracy of the LBA source positions, we compared them to the source positions from the 325 MHz WENSS survey (Rengelink et al. 1997). The positional accuracy of the WENSS survey is reported to be 5″–10″ for the faintest sources and increases to 1.″5 for the brighter sources.

For all our sources detected in the LOFAR images, we searched for the closest counterpart in the WENSS survey. The difference between the LOFAR positions and WENSS positions are displayed in Figure 9. The positional offsets ($\Delta\alpha$, $\Delta\delta$) are a combination of imperfect calibration, noise dependent offsets from position determination using Gaussian fitting by `PyBDSM`, and offsets due to differences in source structure between 325 and 34–62 MHz, related to spectral index variations across the sources and/or differences in resolution between the WENSS and LOFAR images.

The median source position offsets between LOFAR and WENSS are smaller than 1/10th of the beam size for all frequencies, and therefore we do not correct our lists for system-

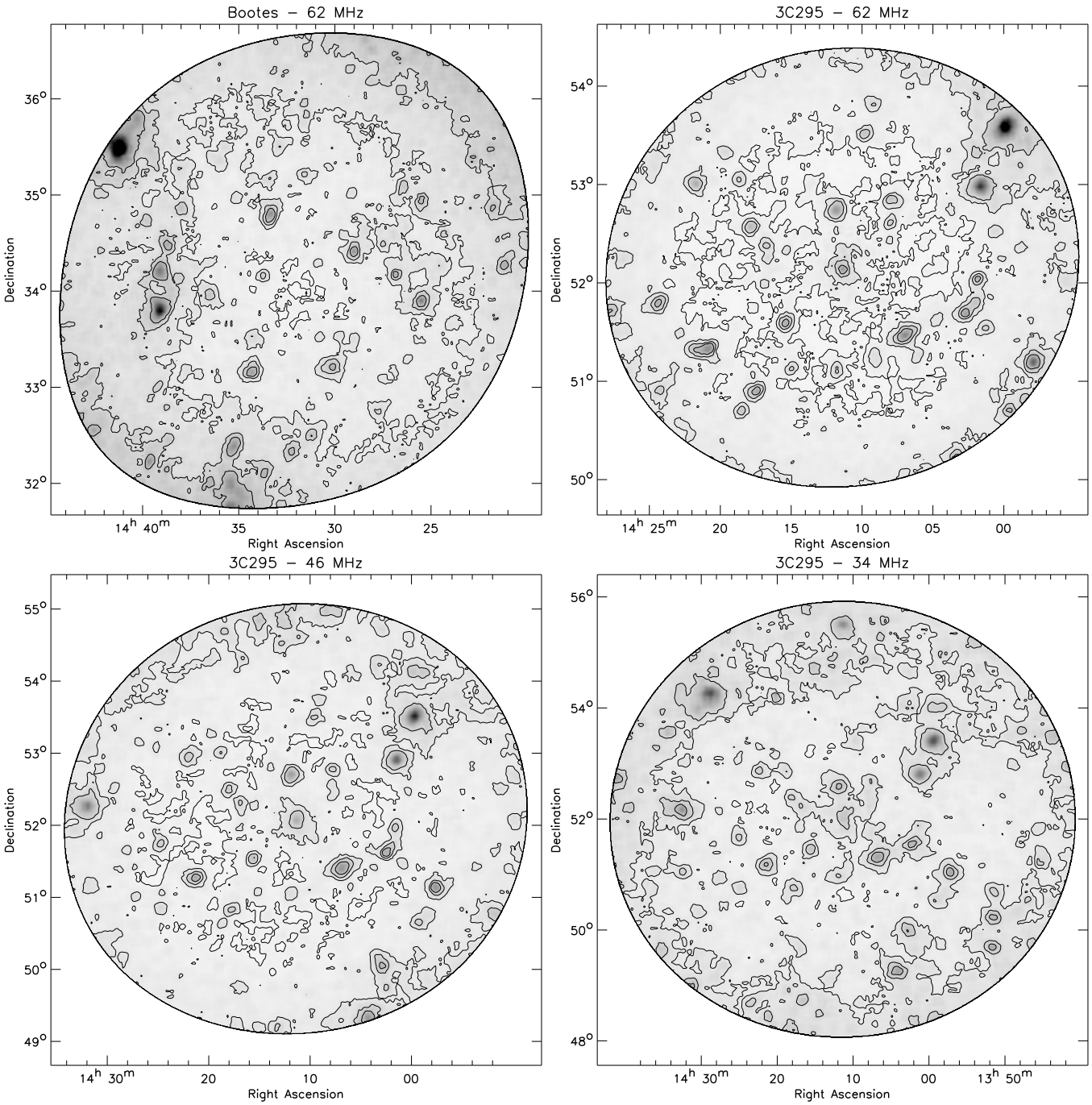

Figure 3. Figures showing the local rms noise in the images. A box size of 80 × 80 pixels was used in computing the local rms noise. The pixel sizes are listed in Table 2. The gray scales display the range from $0.5\sigma_{\rm rms}$ to $10\sigma_{\rm rms}$, with the $\sigma_{\rm rms}$ values taken from Table 2. Contour levels are drawn at $(\sqrt{2})^n \times \sigma_{\rm rms}$, with n ranging from −1 to 3. The local noise variations are correlated with the position of strong sources.

atic position offsets. To reduce the effect of the noise dependent term in the position offsets, we re-calculated the offsets taking only sources that are detected with a signal-to-noise ratio larger than 20 in the LOFAR images. Using only these bright sources, we find a scatter of $(\sigma_\alpha, \sigma_\delta = 1\farcs8, 1\farcs9)_{\rm Bootes,62\,MHz}$, $(\sigma_\alpha, \sigma_\delta = 2\farcs1, 3\farcs1)_{\rm 3C\,295,62\,MHz}$, $(\sigma_\alpha, \sigma_\delta = 3\farcs7, 5\farcs6)_{\rm 3C\,295,46\,MHz}$, and $(\sigma_\alpha, \sigma_\delta = 6\farcs5, 10\farcs2)_{\rm 3C\,295,34\,MHz}$ between LOFAR and WENSS. We added these values in quadrature to the position uncertainties determined from the Gaussian fitting. The strong increase in the scatter toward the lower frequencies suggests that this is the result of residual ionospheric phase errors. The Boötes field has the smallest spread in position offsets.

3.3. Flux Density Uncertainties

For our absolute flux calibration (bootstrapping), we took the scale from Scaife & Heald (2012) for 3C 295. Scaife & Heald report an uncertainty in the 3C 295 flux scale of about 8% at 34 MHz, 6% at 46 MHz, and 4% at 62 MHz.

We performed a check on the accuracy of the beam model and bootstrapping of the flux scale. We did this by checking for flux density variations within the FoV and by looking for an overall scaling factor (which applies to all sources within a field). For this, we compared the measured LBA flux densities to predicted flux densities from external surveys. These predicted

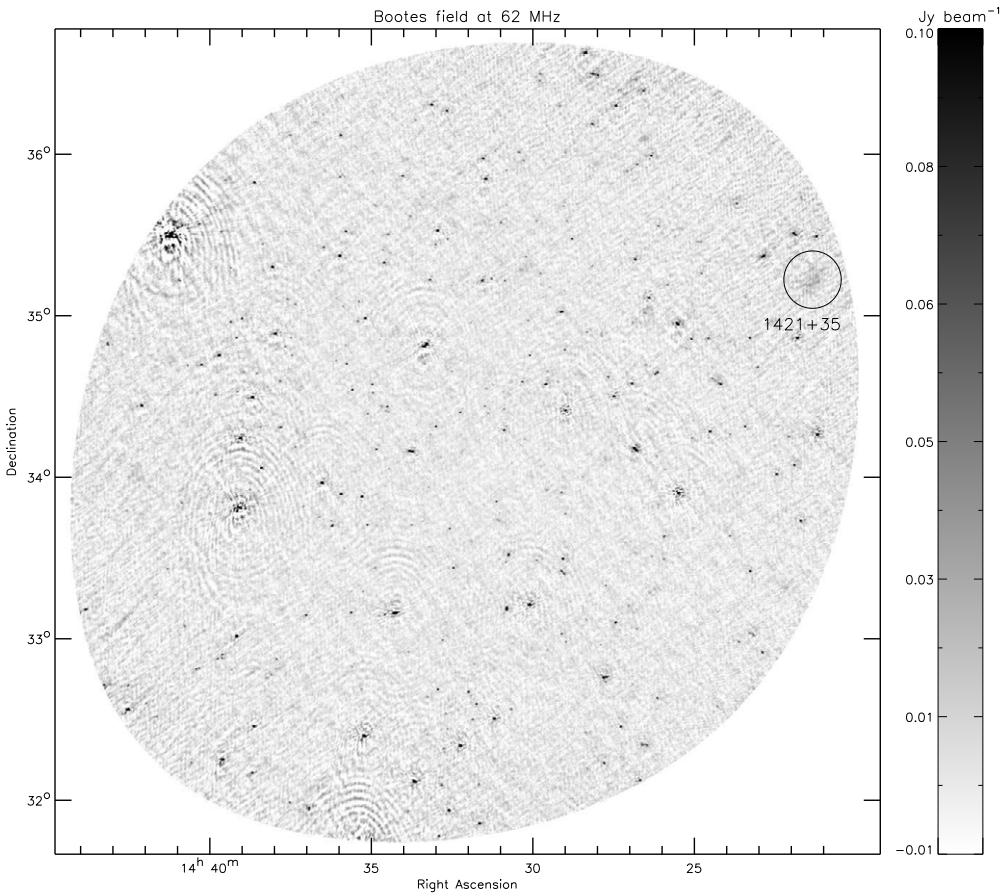

Figure 4. Primary beam corrected Boötes field 62 MHz image. The image is blanked beyond a primary beam attenuation factor of 0.4. The position of the diffuse source 1421+35 is indicated.

Table 3
Combined LOFAR Boötes and 3C 295 Field Source Catalogs

Source ID	R.A. (deg)	$\sigma_{\rm R.A.}$ (arcsec)	Decl. (deg)	$\sigma_{\rm Decl.}$ (arcsec)	$S \pm \sigma_S$ (mJy)
J143859.5+345312	219.74800	2.2	34.88676	2.1	237 ± 40
J143856.4+343310	219.73524	3.2	34.55297	2.5	145 ± 29
J143849.0+335015	219.70420	1.8	33.83753	1.9	6469 ± 1008
J143849.3+341553	219.70580	1.8	34.26481	1.9	2816 ± 439
J143850.4+350020	219.71027	2.0	35.00571	2.0	298 ± 49
J143831.3+335652	219.63057	4.4	33.94792	3.2	174 ± 36
J143828.9+343107	219.62059	1.8	34.51874	1.9	2035 ± 317
J143819.1+321149	219.57987	2.1	32.19706	2.1	566 ± 91
J143831.6+355053	219.63205	2.1	35.84832	2.1	516 ± 81
J143817.1+322905	219.57145	1.8	32.48483	2.0	1251 ± 196
J143821.6+344000	219.59040	2.6	34.66683	2.2	194 ± 34
J143814.2+342010	219.55944	2.8	34.33632	2.2	148 ± 27
J143810.9+340500	219.54543	1.8	34.08339	1.9	797 ± 125
J143814.8+352807	219.56189	2.6	35.46880	2.3	186 ± 32
J143750.2+345451	219.45921	1.8	34.91425	2.1	2106 ± 328

(This table is available in its entirety in a machine-readable form in the online journal. A portion is shown here for guidance regarding its form and content.)

fluxes are based on the NVSS (Condon et al. 1998), WENSS (Rengelink et al. 1997), GMRT 153 MHz (Williams et al. 2013, in the case of the Boötes field only), and VLSS Redux (VLSSr; Lane et al. 2012) surveys. We fitted second-order polynomials to these flux measurements in $\log(S)$–$\log(\nu)$ space. We use these polynomial fits to predict the flux densities at the relevant LBA frequencies. To obtain reliable predictions, we only included LOFAR sources that were detected in all external surveys.

For the Boötes field, we find a scatter of 15% between the measured and predicted 62 MHz fluxes and a mean flux ratio of 0.8 (measured flux divided by predicted flux), see Figure 10. If we use the polynomial fits from NVSS, WENSS, and GMRT

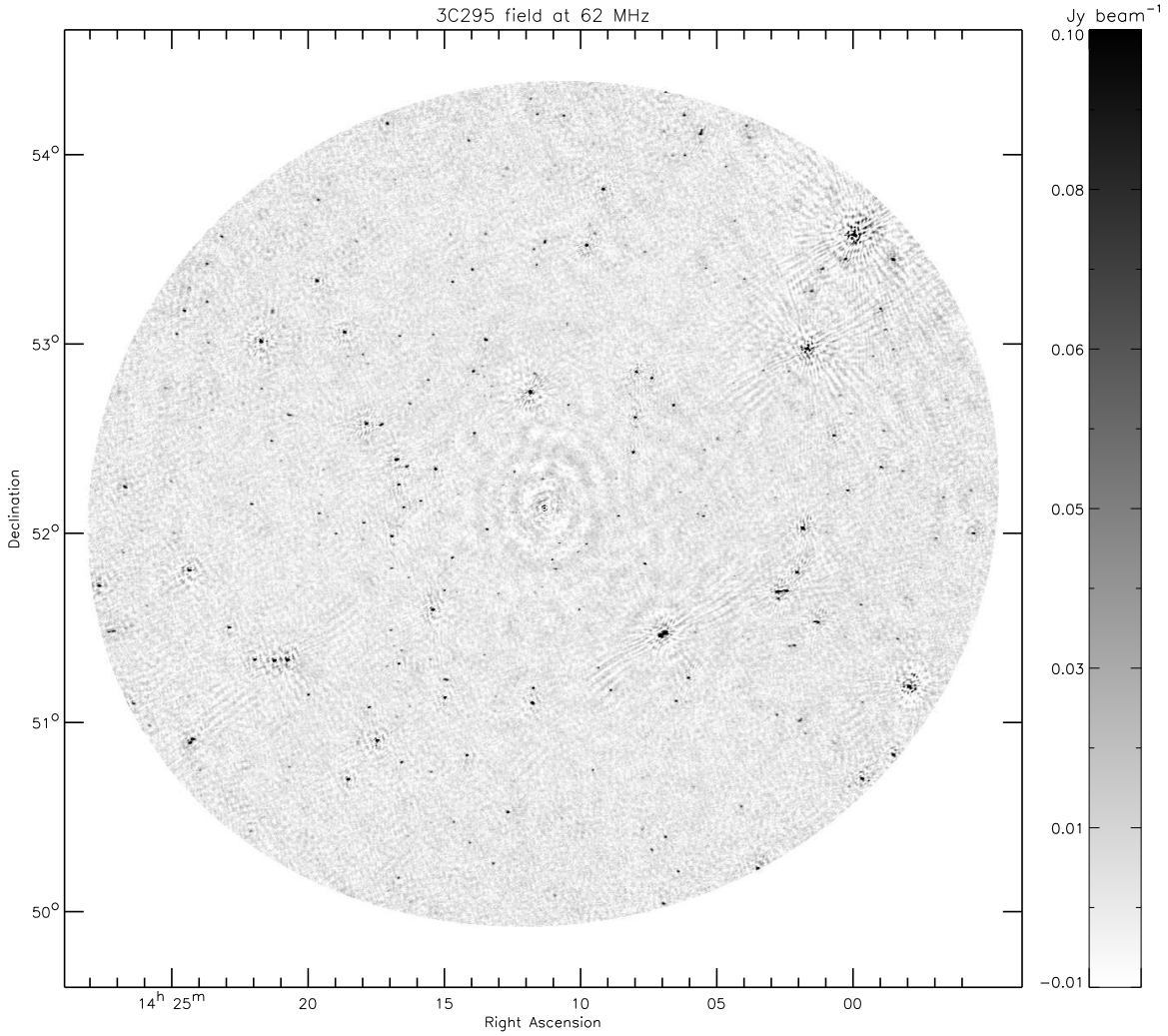

Figure 5. Primary beam corrected 3C 295 field 62 MHz image. The image is blanked beyond a primary beam attenuation factor of 0.4.

153 MHz to predict the VLSSr fluxes we find a scatter of 5%. Therefore, some of the scatter can be attributed to the intrinsic uncertainties in the predicted LOFAR LBA fluxes due to measurement errors. For the 3C 295 field, we find a scatter of 18%, 29%, 48%, at 62, 46, and 34 MHz, respectively. No clear trends with radial distance from the field center are found. The increase in the scatter for the 3C 295 field at 62 MHz, compared to the Boötes field, is not unexpected since we do not have high-quality GMRT 153 MHz flux density measurements available which help to predict the LBA fluxes. In addition, the predicted 46 and 34 MHz flux densities are considerably more uncertain as we extrapolate from higher frequency data. We therefore argue that the Boötes field 62 MHz fluxes are best suited to determine the flux-scale accuracy across the FoV.

The average measured to predicted flux ratios for the 3C 295 field are 1.0, 1.0, and 1.05, at 62, 46, and 34 MHz, respectively. The mean flux density ratios for the 3C 295 field are consistent with the uncertainty in the adopted flux scale for 3C 295 itself, reported by Scaife & Heald (2012). The mean flux ratio of 0.8 for the Boötes field likely resulted from the amplitude transfer from 3C 295 to the Boötes field. This transfer relies on the accuracy of the global beam model. At the time of our observations there were issues with the remote station processing (RSP) boards, which could have affected the beam shapes and sensitivities of some stations, resulting in errors when transferring the flux scale from one pointing to another. The RSP boards were fixed about half a year after our observations.

From the above results, we conclude that the relative uncertainties in the flux scale within a single FoV due to uncertainties in the beam model are likely less than 15%. We note that this 15% refers to the averaged beam model of all stations over the entire period of the observations. This result is similar to the ∼10% we found for LBA observations of A2256 (van Weeren et al. 2012). The transfer of the flux scale from one field to the other (i.e., from calibrator to target) seems to be more uncertain, in our case we find a mean ratio of 0.8 (Figure 10). To bring the Boötes field flux densities to the same scale as the 3C 295 field, we multiplied them by a factor of 1.25.

The integrated flux density errors (σ_S, Equation (3)) are thus a combination of the uncertainties from 3C 295 flux scale, the uncertainties from the Gaussian fitting ($\sigma^2_{\rm gauss}$), and a conservative 15% uncertainty to account for the beam model

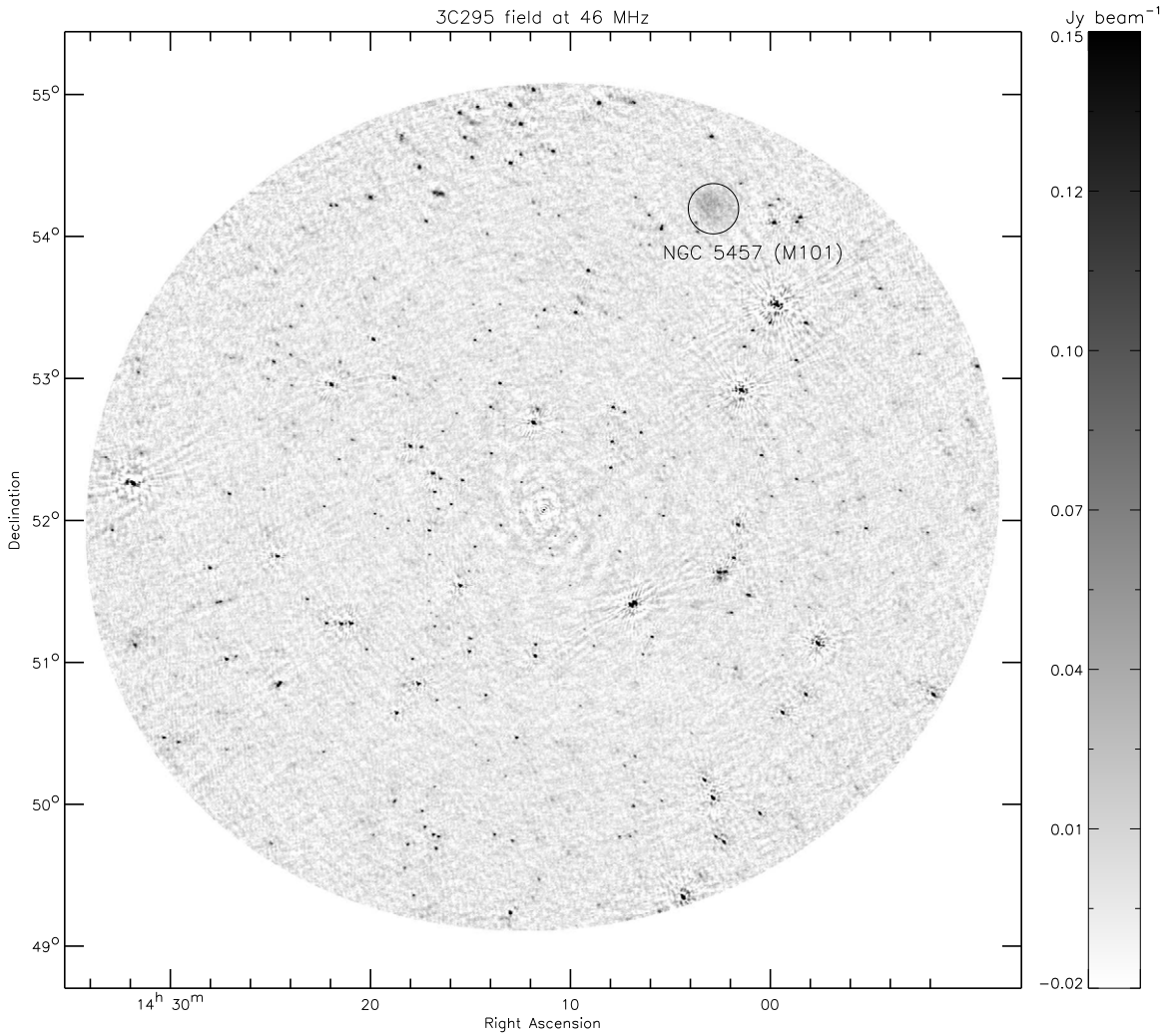

Figure 6. Primary beam corrected 3C 295 field 46 MHz image. The image is blanked beyond a primary beam attenuation factor of 0.4. The position of NGC 5457 is indicated.

used during the imaging process:

$$\sigma_S^2 = \begin{cases} (0.04S)^2 + \sigma_{\rm gauss}^2 + (0.15S)^2 & 62\,{\rm MHz} \\ (0.06S)^2 + \sigma_{\rm gauss}^2 + (0.15S)^2 & 46\,{\rm MHz} \\ (0.08S)^2 + \sigma_{\rm gauss}^2 + (0.15S)^2 & 34\,{\rm MHz} \end{cases}. \quad (3)$$

In addition, averaging over a wide frequency range leads to an additional flux density error that depends on spectral index of the source. In this work, we neglect this error as it is smaller than 1% for a source with $\alpha = -1$.

3.4. Completeness and Reliability

To quantify the completeness and reliability of the source lists, we performed a Monte Carlo (MC) simulation in which we generated 25 random fields corresponding to each LOFAR image. Each field contains $\sim$ 1200 randomly positioned point sources with peak flux densities between 2.5 mJy and 6.3 Jy (the catalog range) for the Boötes 62 MHz field, 2.3 mJy and 6.6 Jy for the 3C 295 62 MHz field, 3.9 mJy and 8.3 Jy for the 3C 295 46 MHz field, and 8.9 mJy and 8.0 Jy for the 3C 295 34 MHz field. The source flux densities are drawn randomly from the source count distribution, $dN/dS \propto S^{-1.6}$ (Williams et al. 2013). We neglect the deviation of the true source counts from a power-law slope at high flux densities because there are very few sources at these flux densities. The effect of the beam is naturally taken into account by inserting sources in the noise-inhomogeneous maps. We also deal with non-Gaussian noise (calibration errors) in this way. Our MC simulation also accounts for the strong ionospheric and bandwidth smearing in the real LOFAR images by scaling the size of the point sources with radial distance from the center of the field. The radial scaling factor is determined by the median value within radial distance bins of the ratio of the measured fitted major axes to the beam major axis in each field. For comparison, we also ran the MC simulation without any smearing. Simulated sources were inserted into the residual images resulting after source detection with `PyBDSM`. Source detection was performed for each randomly simulated field in the same manner as described in Section 3.1. Only $\sim$300–400 sources in each field satisfy the detection criterion of peak flux density $>5\sigma$.

We have estimated the catalog completeness by plotting the fraction of detected sources in our MC simulation as a function of integrated flux density (left panel of Figure 11), i.e., the fraction of input sources that have a catalog flux density using the same detection parameters. The completeness at a

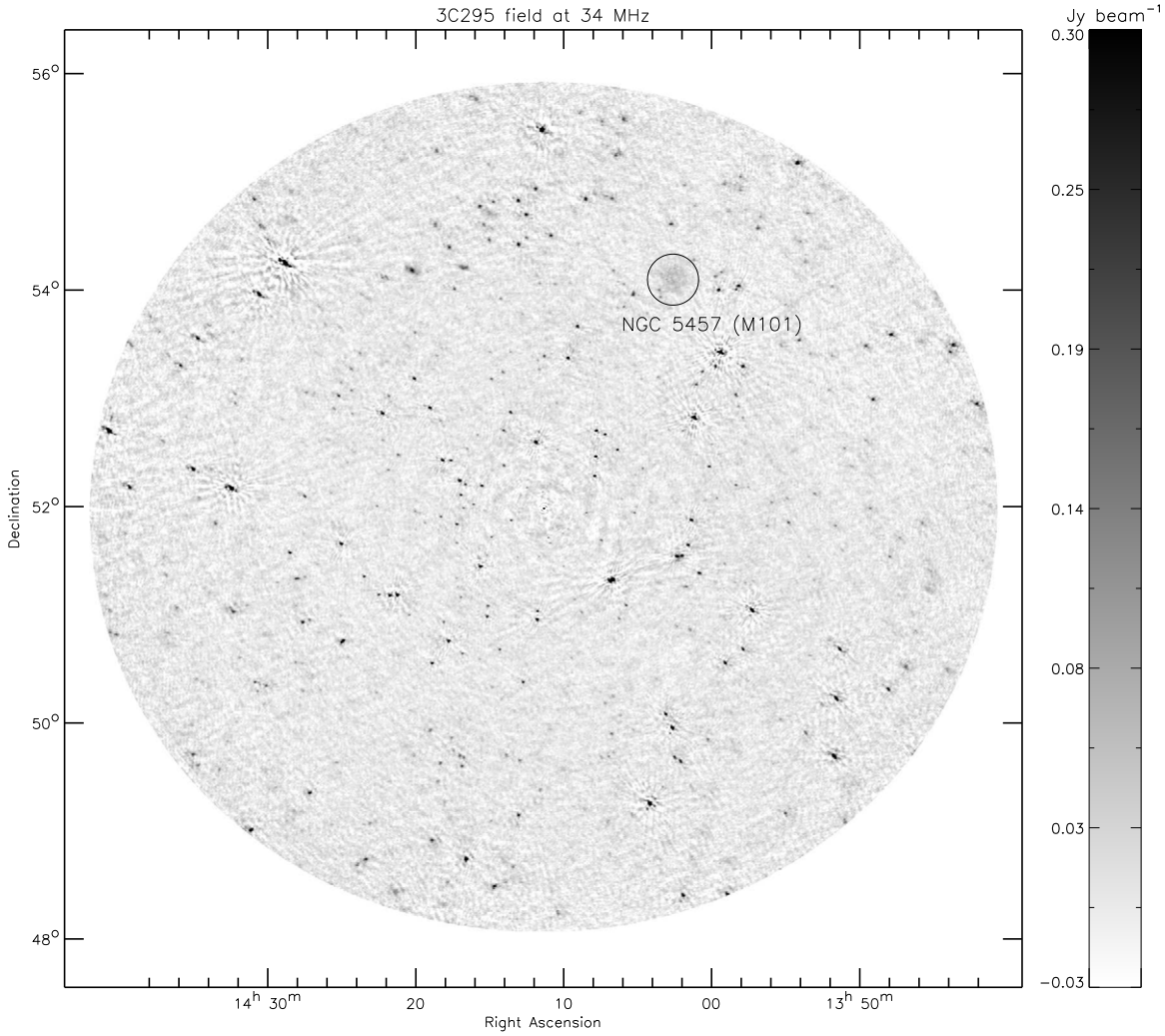

Figure 7. Primary beam corrected 3C 295 field 34 MHz image. The image is blanked beyond a primary beam attenuation factor of 0.4. The position of NGC 5457 is indicated.

given flux density is determined by integrating the detected fraction upwards from a given flux density limit and is plotted as a function of integrated flux density in right panel of Figure 11. Due to the variation in the rms noise across the image, the detection fraction has first been multiplied by the fraction of the total area in which the source can be detected. We thus estimate that the catalog is 95% complete above a peak flux density of 37 mJy (Boötes 62 MHz) and 88 mJy, 51 mJy, and 30 mJy (3C 295 34, 46, and 62 MHz, respectively).

The reliability of the catalog indicates how many sources above a given flux density are real. In the left panel of Figure 12, the false detection rate (FDR), i.e., the fraction of catalog sources that do not have an input source, is plotted as a function of the integrated flux density. Integrating up from a given limit and multiplying by the normalized source flux distribution, we can determine an estimate of the overall FDR or reliability, $R = 1 - \mathrm{FDR}$, of the catalog. The reliability is plotted as a function of integrated flux density limit in the right panel of Figure 12. We thus estimate that the source list is 95% reliable above a peak flux density of 42 mJy (Boötes 62 MHz) and 108 mJy, 53 mJy, and 32 mJy (3C 295 34, 46, and 62 MHz, respectively). These estimates include source smearing.

4. ANALYSIS

4.1. Source Counts

We use the source lists to compute the Euclidean-normalized source counts at 62, 46, and 34 MHz. For this, we have to take into account the large variations of the rms noise across the images (e.g., Windhorst et al. 1985). We choose the flux density bin sizes such that we have approximately 30–60 sources per bin, except for the first and last bins. We corrected these source counts using the MC simulations described in Section 3.4 with the detected fraction of sources as a function of flux density. The propagated errors in the source counts are based on the Poissonian uncertainties and the uncertainties in the derived detection fraction, see Table 4. The resulting Euclidean-normalized source counts are shown in Figures 13 and 14.

Only a few source count studies exist below 100 MHz. Cohen et al. (2003, 2004) and Tasse et al. (2006) published source counts at 74 MHz with the VLA. We compare our source counts with those from Cohen et al. (2004) and Tasse et al. (2006) because they go to fainter flux densities than those from Cohen et al. (2003). For that comparison, we rescale the Cohen et al. (2004) and Tasse et al. (2006) flux densities to the newly adopted VLSSr flux scale (Lane et al. 2012). The VLSSr counts are included as well (Lane et al. 2014). We also compare with

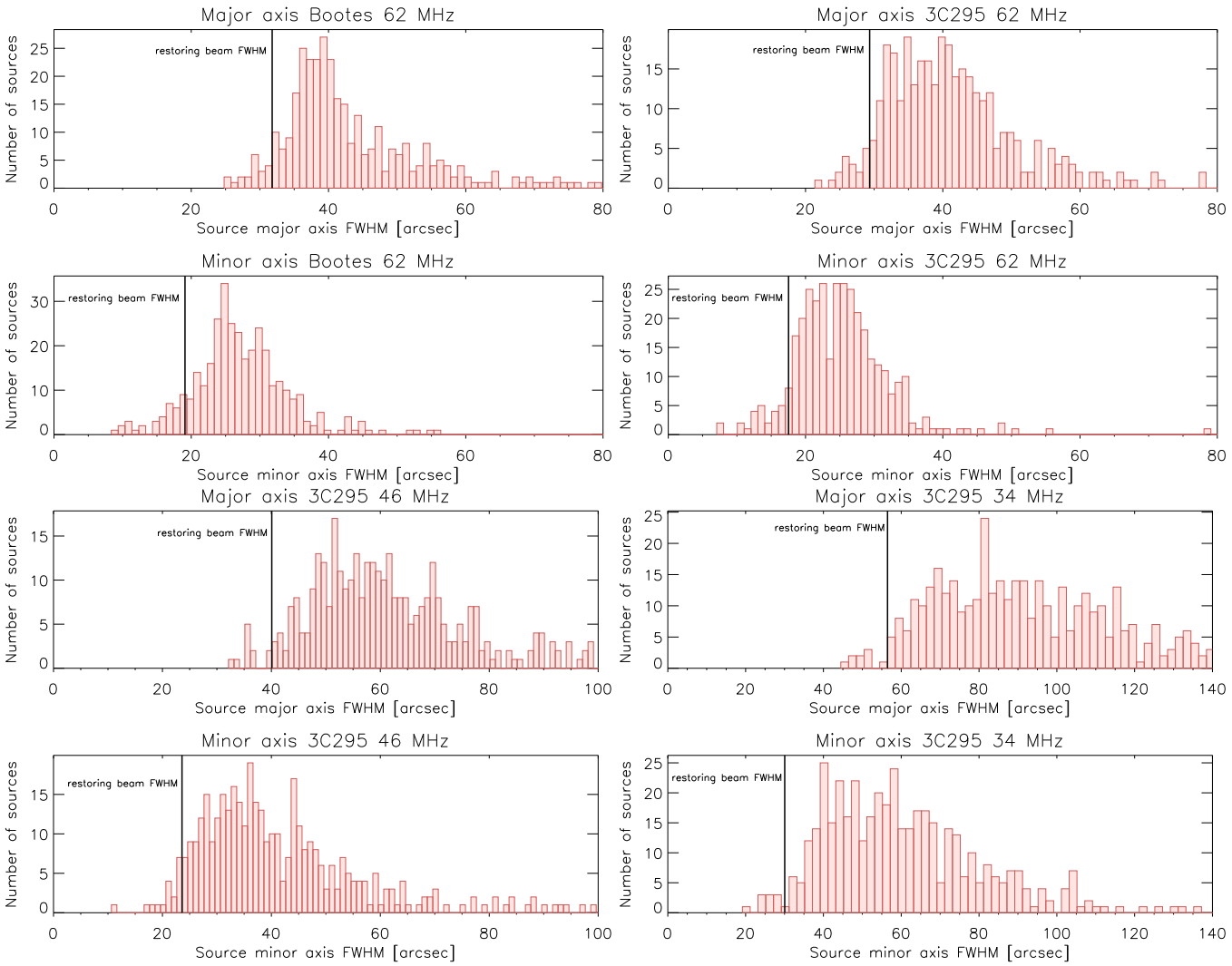

Figure 8. Distribution of fitted major and minor axes (FWHM) for the Boötes and 3C 295 fields. These values are not deconvolved by the beam. Solid black line indicates the fitted restoring beam based on the uv coordinates. Uncorrected ionospheric phase variations causes "smearing" of sources and decreases the effective resolution. This effect increases toward lower frequencies.

(A color version of this figure is available in the online journal.)

153 MHz source counts from the GMRT for the Boötes field (Williams et al. 2013) because it overlaps to a large extent with our Boötes field data.

The combined source counts at 62 MHz from the Boötes and 3C 295 fields show very good agreement with the results at 74 MHz, which are scaled using $\alpha = -0.7$. The 62 MHz counts reach significantly fainter (about a factor of six), flux density levels than the 74 MHz counts. The 62 MHz counts fall slightly below the GMRT 153 MHz counts, if we scale these with a spectral index of -0.7. The simulated 151 MHz SKAD S^3-SEX counts (Wilman et al. 2008) closely follow the GMRT 153 MHz counts.

The 34 MHz source counts fall significantly below the extrapolated source counts from 153 and 74 MHz if we scale with $\alpha = -0.7$. This is also the case for the simulated 151 MHz SKAD S^3-SEX counts. The 46 MHz differential source counts show a similar situation, although the difference is most pronounced below 0.5 Jy. Scaling with $\alpha = -0.5$ gives a better agreement with the 34 and 46 MHz source counts, an indication that the average spectral index of the sources flattens toward lower frequencies, a result that has been reported before (e.g., Lacy et al. 1992). However, part of the difference could also be caused by field to field variations (Heywood et al. 2013). To check this, we compared the separate source counts for the two fields at 62 MHz, instead of the combined counts that are shown in Figure 13. We find that the 3C 295 field source counts are generally about 20%–30% lower than for the Boötes field (see Figure 19), so this could explain some of the difference.

Spectral flattening is expected for some sources because of absorption effects and low-frequency spectral indices are flatter than high-frequency ones due to spectral ageing operating at higher frequencies. We note though that our flux reference 3C 295 also incorporates a strong spectral turnover below ~60 MHz and hence we have to be careful to conclude whether the flattening is intrinsic or is caused by our uncertain calibrator flux scale. Fortunately, the 8C 38 MHz counts allow for a more direct comparison at flux densities above ~1 Jy (Rees 1990; Hales et al. 1995). We find good agreement between our 34 MHz sources counts and those from the 8C survey. In addition, the 8C counts match up with the extrapolated counts from the VLSSr (at 74 MHz) and the GMRT (at 153 MHz) using a spectral index scaling of $\alpha = -0.5$. The 8C source counts at 38 MHz are not

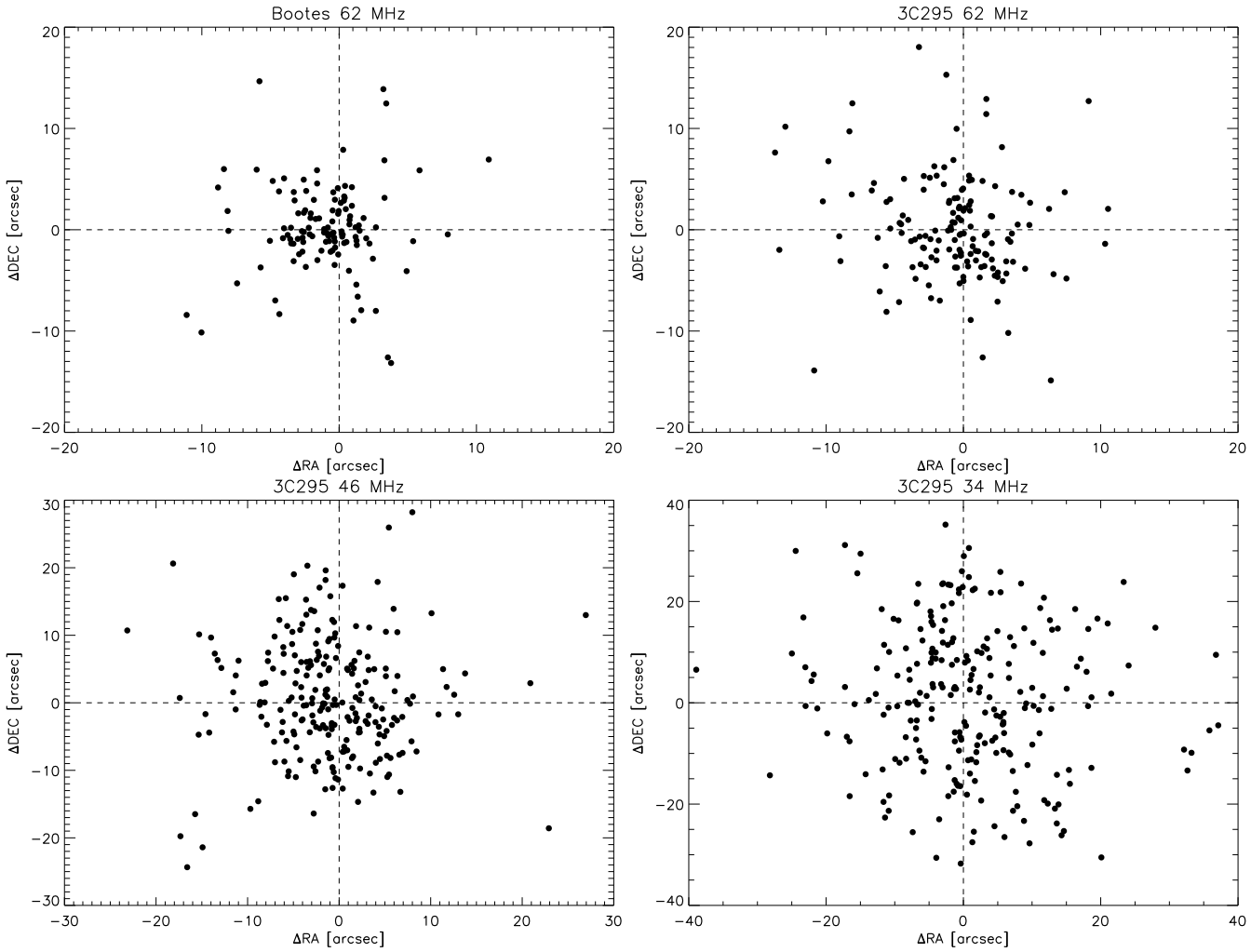

Figure 9. Position offsets between the LOFAR LBA and the 325 MHz WENSS sources.

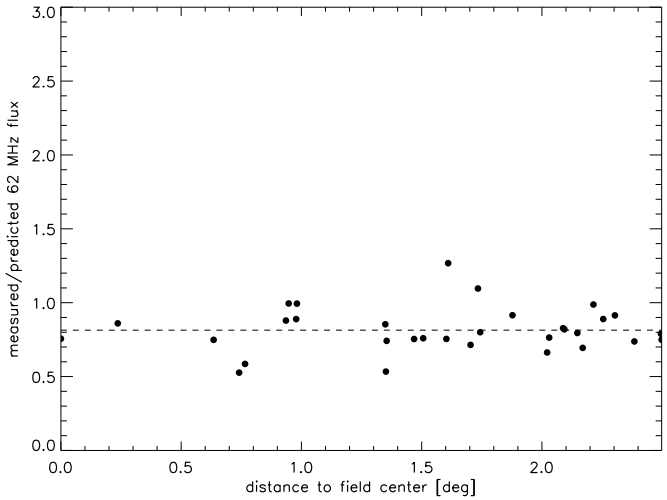

Figure 10. Measured flux densities over the predicted flux densities as function of radial distance to the Boötes field center. Dashed line shows the robust mean of the plotted data points.

consistent with the VLSSr and GMRT counts if we scale with a spectral index of $\alpha = -0.7$. This indeed shows that on average the spectral indices of sources flatten. It is important to note that the VLSSr and 8C counts are not affected by field to field variations given the large sky area they cover.

4.2. Spectral Indices

In the above section, we found evidence for spectral flattening of sources toward lower frequencies. In this subsection we investigate the spectral properties of the detected LBA sources.

For the Boötes field sources, we search for counterparts in the NVSS and GMRT 153 MHz catalogs using a matching radius of 20″. If more than one counterpart to a 62 MHz source is found we add up the flux of all counterparts within the 20″ radius. In Figure 15, we plot α_{62}^{1400} against the 62 MHz flux density. From this we find an average spectral index of −0.79. This average drops to −0.74 for α_{62}^{153} and increases to −0.81 for α_{153}^{1400}. The average spectral index between 1400 and 153 MHz we find is within the range of previously reported values: −0.87 (Williams et al. 2013), −0.79 (Intema et al. 2011), −0.78 (Ishwara-Chandra et al. 2010), −0.82 (Sirothia et al. 2009), and −0.85 (Ishwara-Chandra & Marathe 2007).

We compute the same values for the 3C 295 field, but starting with the 34 MHz source catalog. We find an average spectral index of −0.81 between 1400 and 34 MHz for the sources. This decreases to −0.85 between 1400 and 62 MHz and increases to −0.64 between 62 and 34 MHz, indicating that the average spectral index flattens toward lower frequencies. The value of −0.64 is somewhat steeper than the −0.5 suggested by the source count scalings.

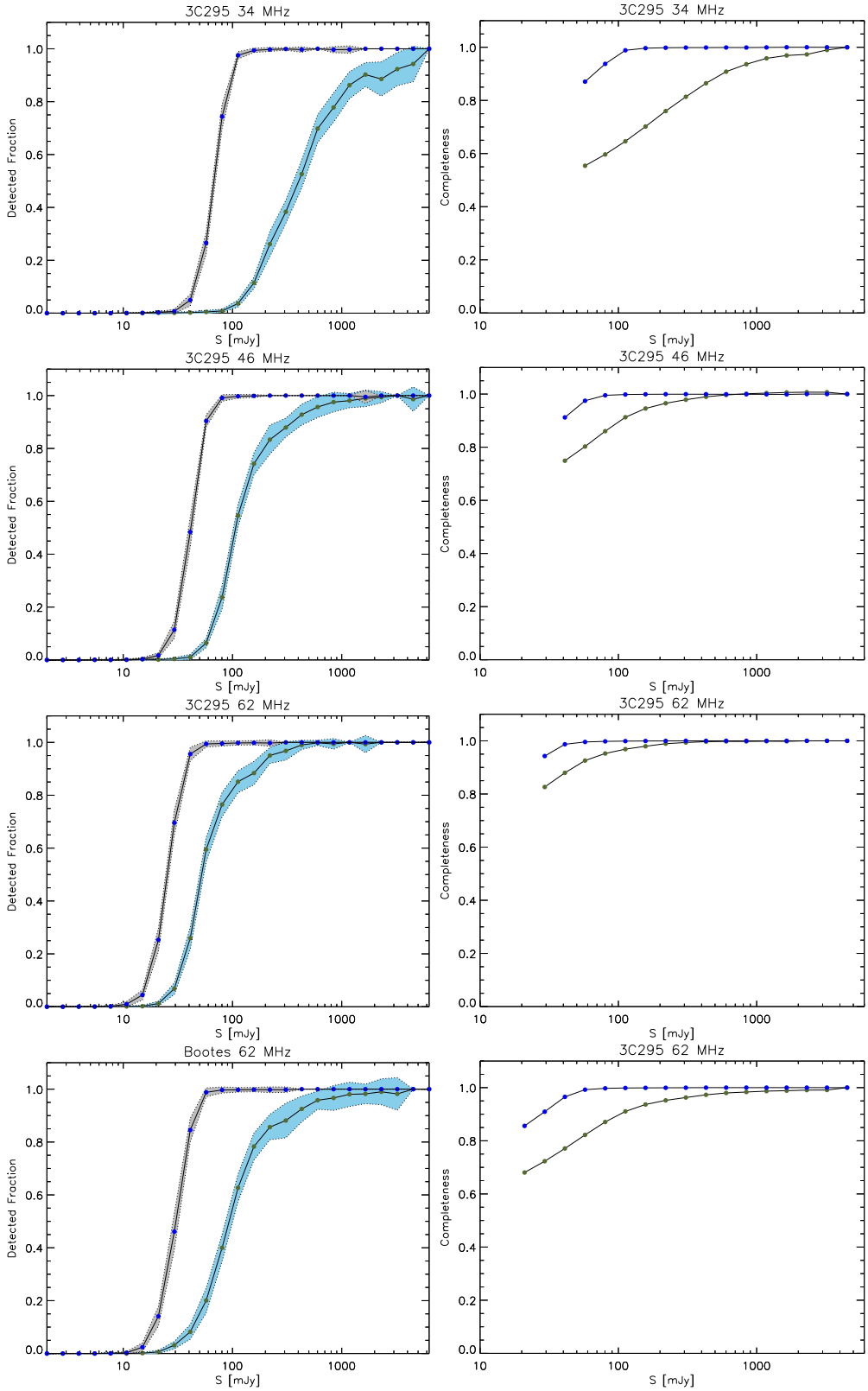

Figure 11. Detection fraction and completeness. From top to bottom: 3C 295 34, 46, and 62 MHz and Boötes 62 MHz. Left: fraction of sources detected as a function of integrated flux density calculated from 25 Monte Carlo (MC) simulations. The solid line shows the mean of all 25 randomly generated fields and the shaded areas show the 1σ uncertainty. The blue shaded areas and olive points include source smearing in the MC simulations (see the main text of Section 3.4). The gray shaded areas and blue points do not include source smearing. Right: estimated completeness of the catalog as a function of integrated flux density limit accounting for the varying sensitivity across the field of view. The olive points include source smearing, the blue points do not.

(A color version of this figure is available in the online journal.)

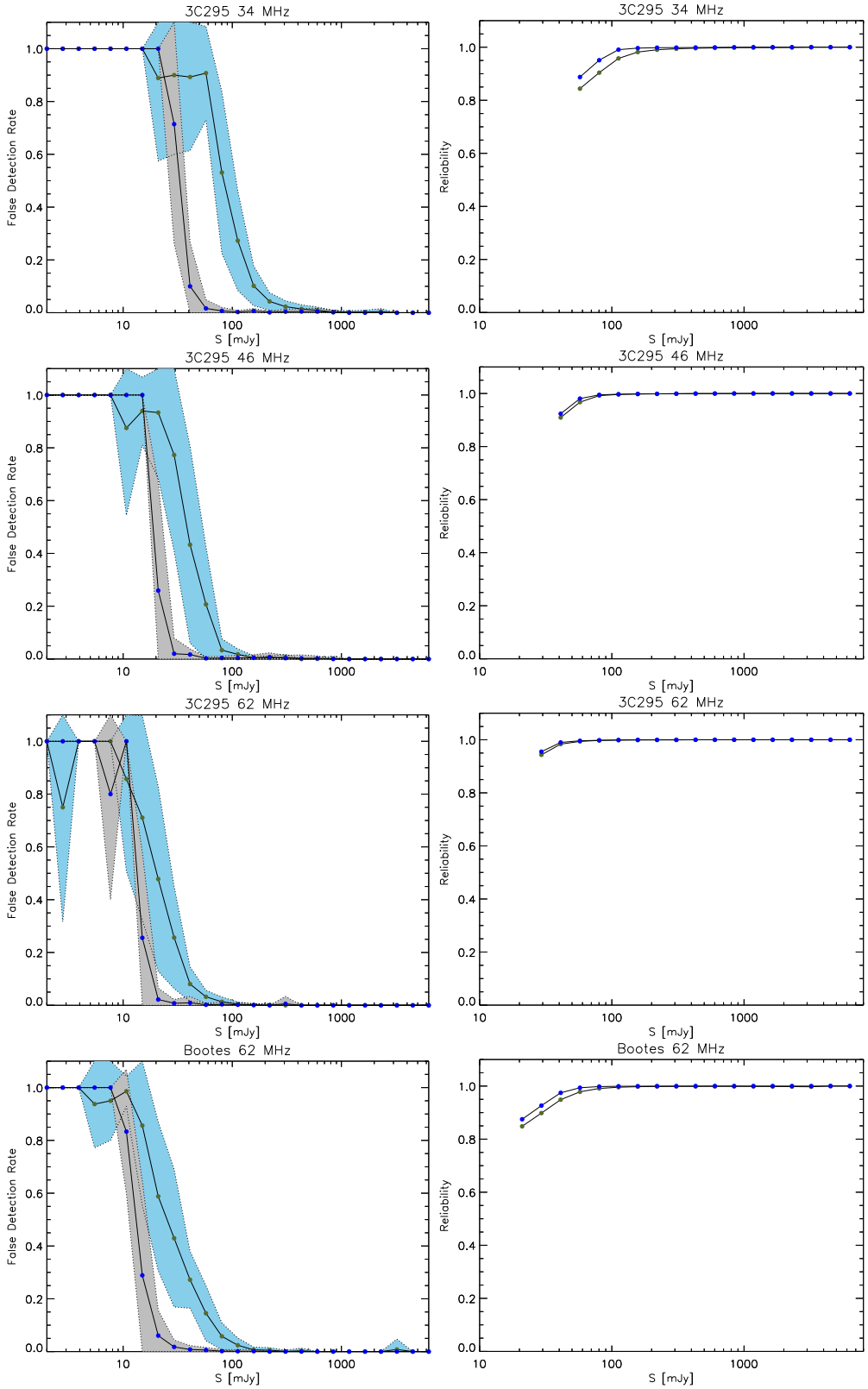

Figure 12. False detection rate and reliability. From top to bottom: 3C 295 34, 46, and 62 MHz and Boötes 62 MHz. Left: false detection rate as a function of peak flux density to local signal-to-noise ratio calculated from 25 Monte Carlo (MC) simulations. The solid line shows the mean of all 25 randomly generated fields and the shaded areas show the 1σ uncertainty. The blue shaded areas and olive points include source smearing in the MC simulations (see main the text of Section 3.4). The gray shaded areas and blue points do not include source smearing. Right: estimated reliability of the catalog as a function of integrated flux density limit accounting for the varying sensitivity across the field of view. The olive points include source smearing, the blue points do not.

(A color version of this figure is available in the online journal.)

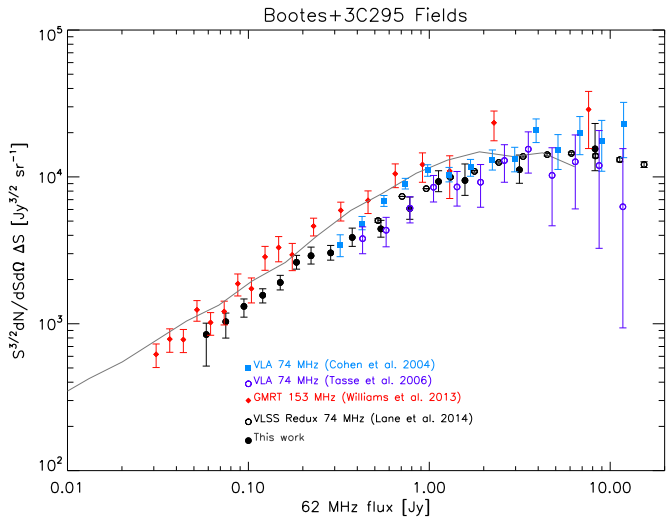

Figure 13. Euclidean-normalized differential source counts at 62 MHz combining the Boötes and 3C 295 fields. The LOFAR points are indicated by the black symbols. Red diamonds are Boötes field source counts at 153 MHz, scaled to 62 MHz using $\alpha = -0.7$. Black open circles, blue squares, and purple open circles are 74 MHz differential source counts from Tasse et al. (2006), Cohen et al. (2004), and Lane et al. (2014) and the solid gray line displays the counts from the 151 MHz SKADS S^3-SEX simulation (Wilman et al. 2008). These are all scaled to 62 MHz assuming $\alpha = -0.7$.

(A color version of this figure is available in the online journal.)

For the brighter, $S_{34} \gtrsim 1$ Jy, 34 MHz sources, we also fitted the radio spectra with a second-order polynomial ($\log_{10}(S) = a_0 + a_1 \log_{10}(\nu) + a_2(\log_{10}(\nu))^2$), including the flux densities from the VLSSr, WENSS, and NVSS surveys. In total we compute spectra for 27 sources, basically all 34 MHz sources that have a counterpart in the VLSSr survey (the VLSSr survey has a rms noise level of $\sim$0.1 Jy beam^{-1}). From the polynomial fits, we derive the spectral curvature between 500 and 50 MHz, i.e., the difference in the slope (spectral index) between 50 and 500 MHz. The resulting histogram is displayed in Figure 15 (right panel). The histogram shows an excess of sources with curved spectra. We find that 14 sources have curved spectra ($a_2 < -\sigma_{a_2}$, where σ_{a_2} is the uncertainty in a_2), while 13 other sources have fits that are consistent with straight (power-law) spectra. None of these sources had an inverted spectrum, with $a_2 > \sigma_{a_2}$. The average spectral curvature of 0.3 is consistent with the increase of the average spectral index from $\alpha_{153}^{1400} = -0.85$ to $\alpha_{34}^{62} = -0.64$ that we found earlier. This average was based on 133 sources so it shows that the spectral flattening is not only confined to the 27 brighter ($S_{34} \gtrsim 1$ Jy) 34 MHz sources.

4.3. Ultra-steep Spectrum Sources

A large number of deep surveys at multiple wavelengths are available that cover the Boötes field, particularly at radio wavelengths. We therefore carried out a search for sources which have USS to select candidate HzRGs. USS sources that are detected at low frequencies could be missed by the higher frequency WENSS and/or NVSS survey due to their steep spectra. We therefore selected all sources detected at 62 and 153 MHz (from Williams et al. 2013), but that are missed in either the WENSS or NVSS survey. In total, we find five of these sources, see Table 5. In addition, we selected sources from the 62 MHz source list that satisfied the criteria $\alpha_{62}^{153} < -1.1$ and $\alpha_{153}^{1400} < -1.1$, since a large part of our field overlaps with the deep 1.4 GHz Westerbork Synthesis Radio Telescope survey of the Boötes field from de Vries et al. (2002), which can be used to compute the spectral indices. Three additional sources were found in this way (Table 5).

Croft et al. (2008) also searched for HzRGs in the Boötes field. They selected candidate HzRGs with $S_{1400} > 1$ mJy in a matched 325 MHz/1.4 GHz sample. The five sources with the steepest radio spectra and without optical counterparts were followed up with deep K-band imaging. None of the sources listed in Table 5 are reported by Croft et al. (2008), as all but one of the sources from Croft et al. have $\alpha_{325}^{1400} > -1.0$.

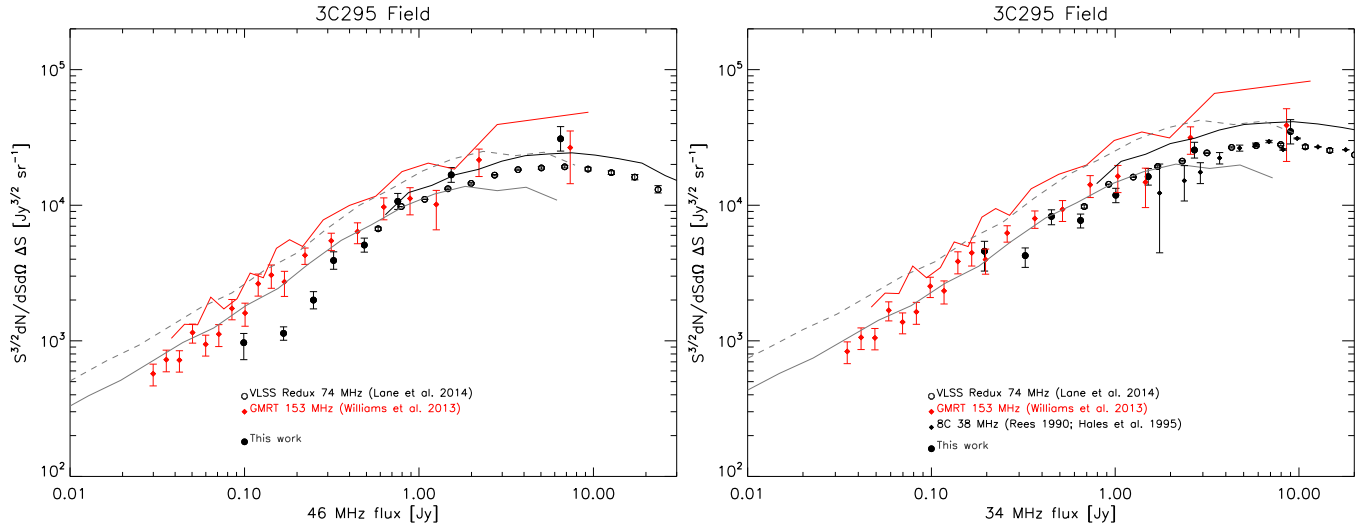

Figure 14. Euclidean-normalized differential source counts at 46 (left) and 34 MHz (right) for the 3C 295 field. The LOFAR points are indicated by the black circles. The red diamonds are Boötes field source counts at 153 MHz and the black open circles show the VLSSr counts at 74 MHz (Lane et al. 2014), both scaled with $\alpha = -0.5$. Red and black solid lines show the same source counts but scaled with $\alpha = -0.7$. The solid and dashed gray lines display the counts from the 151 MHz SKADS S^3-SEX simulation (Wilman et al. 2008) scaled with $\alpha = -0.5$ and $\alpha = -0.7$, respectively. For the 34 MHz panel we have also plotted the 8C source counts at 38 MHz with black diamonds. The 8C source counts are complete to a flux level of about 5 Jy. Below a flux density of 5 Jy, we have corrected the source counts using the information provided in Figure 7 from Rees (1990).

(A color version of this figure is available in the online journal.)

Table 4
Source Counts

Flux Bin (Jy)	Raw Counts	Corrected Counts	Normalized Counts ($Jy^{3/2}$ sr^{-1})
62 MHz Boötes+3C 295			
0.051–0.066	32	181	844^{+164}_{-329}
0.066–0.084	47	143	1032^{+150}_{-234}
0.084–0.105	51	119	1312^{+162}_{-204}
0.105–0.135	62	111	1562^{+167}_{-175}
0.135–0.165	52	78	1909^{+226}_{-210}
0.165–0.204	65	83	2621^{+300}_{-267}
0.204–0.240	45	53	2904^{+422}_{-354}
0.240–0.330	65	75	3037^{+376}_{-327}
0.330–0.420	44	49	3869^{+612}_{-505}
0.420–0.660	55	59	4424^{+634}_{-538}
0.660–0.900	31	32	$6087^{+1,206}_{-945}$
0.900–1.35	36	37	$9295^{+1,716}_{-1,367}$
1.35–1.80	16	16	$9456^{+2,792}_{-1,975}$
1.80–4.50	20	20	$11175^{+2,899}_{-2,132}$
4.5–12.0	7	7	$15509^{+7,595}_{-4,491}$
46 MHz 3C 295			
0.072–0.126	27	155	969^{+165}_{-242}
0.126–0.208	46	76	1136^{+132}_{-127}
0.208–0.288	39	48	1998^{+308}_{-278}
0.288–0.360	38	44	3913^{+622}_{-542}
0.360–0.612	65	72	5087^{+637}_{-577}
0.612–0.900	55	54	$10686^{+1,535}_{-1,367}$
0.900–2.16	66	68	$16747^{+2,218}_{-1,994}$
2.16–10.8	23	23	$30898^{+7,133}_{-5,812}$
34 MHz 3C 295			
0.136–0.252	40	505	4615^{+843}_{-1323}
0.252–0.396	50	163	4257^{+591}_{-773}
0.396–0.504	51	105	8270^{+984}_{-1090}
0.504–0.792	63	105	7726^{+883}_{-927}
0.792–1.22	61	80	$11864^{+1,467}_{-1,422}$
1.22–1.80	46	53	$16252^{+2,409}_{-2,178}$
1.80–3.60	55	61	$25548^{+3,574}_{-3,262}$
3.60–14.4	23	25	$34940^{+7,840}_{-6,624}$

The source with the steepest spectral index from Croft et al. (J142631+341557) is not detected in our LOFAR 62 MHz image. The source is detected at 153 MHz with an integrated flux of 20 ± 5 mJy, giving $\alpha_{153}^{1400} = -1.3$.

For the USS sources, we identify candidate counterparts in the NOAO Deep Wide-Field Survey (NDWFS) *I*-band images. For the optical identification, we use the likelihood ratio technique (Sutherland & Saunders 1992; Tasse et al. 2008). In this way we obtain a probability $P(i)$ that candidate i is the true optical counterpart to a given radio source. For the radio position, we take the GMRT 153 MHz position or, when available, the 1.4 GHz FIRST position. We then obtain flux measurements for all candidate counterparts (with $P(i) > 5\%$) from the NDWFS (B_W, R, I, K; Jannuzi & Dey 1999), the Flamingos Extragalactic Survey (J, K_s; Elston et al. 2006), the zBootes survey (z'; Cool 2007), the *Spitzer* Deep Wide Field Survey ([3.6], [4.5], [5.8], [8.0]; Ashby et al. 2009), *Galaxy Evolution Explorer* GR5 (NUV, FUV; Morrissey et al. 2007), and the MIPS AGN and Galaxy Evolution Survey ([24]; Jannuzi et al. 2010) to obtain photometric redshifts ($z_{\rm phot}$). For the spectral energy distribution (SED) and $z_{\rm phot}$ fitting, we require measurements in at least five bands. The fitting is performed using both the LRT code from Assef et al. (2008) and EAZY[55] (Brammer et al. 2008) for comparison. A much more extensive description of the radio counterpart identification and SED fitting will be given in W. L. Williams et al. (in preparation). The results of the fitting are summarized in Table 6. Figures showing the SEDs for each source and *I*-band, IRAC 4.5 μm, IRAC 8.0 μm, and MIPS 24 μm postage stamps, with GMRT (and FIRST where there is a source) contours, are shown in Appendix B.

We find that the photometric redshifts of the sources are mostly in the $0.7 \lesssim z_{\rm phot} \lesssim 2.5$ range. Given the correlation between optical brightness and redshift, counterparts without photo-z's are likely located at a higher redshift. For J143127.4+343506 and J143345.9+353856, the differences between the EAZY and LRT codes are substantial. We note that the LRT code is supposed to do a better job of fitting AGN and LRT also takes into account the upper limits. Larger USS samples are needed to detect more distant objects as they are more rare. However, steep-spectrum selection also misses a significant fraction of HzRGs (e.g., Jarvis et al. 2009) and not all USS sources are associated with HzRGs (e.g., Jarvis et al. 2001; Cruz et al. 2007; van Weeren et al. 2009). Therefore a combination of deep radio and optical/NIR survey data will be a more powerful way of identifying HzRGs by searching for optically/NIR faint counterparts to the radio sources (e.g., Brookes et al. 2006; Ker et al. 2012).

5. CONCLUSIONS

We have presented the results of LOFAR LBA observations of the Boötes and 3C 295 fields. In our 62 MHz Boötes field image, with a central noise level of 4.8 mJy beam^{-1}, we detect a total of 329 sources over a 19.4 deg^2 area. Our images of the 3C 295 field cover an area from 17 to 52.3 deg^2 from 62 to 34 MHz, respectively. We reach central noise levels of 5.3, 8.2, and 12 mJy beam^{-1} at 62, 46, and 34 MHz for the 3C 295 field. In total we detect 329, 367, and 392 sources at 62, 46, and 34 MHz.

From our source lists, we derive the deepest differential source counts at 62, 46, and 34 MHz to date. At 62 MHz, the source counts are in good agreement with 74 MHz counts from VLA observations and scaling with a spectral index of -0.7. At 34 MHz, the measured source counts fall significantly below extrapolated source counts from 74 and 153 MHz, using a spectral index scaling of -0.7. Instead, we find that a spectral index scaling of -0.5 provides a better match to the observed 34 MHz source counts. Our 34 MHz source counts are also consistent with those obtained from the 38 MHz 8C survey. In addition, evidence for spectral flattening is found from the increase of the average radio spectral index from high to low frequencies. From polynomial fits to the individual flux densities of bright ($\gtrsim$1 Jy) 34 MHz sources, we conclude that about half of these sources have curved spectra. The curved spectra of these sources could be caused by absorption effects as well as by spectral ageing.

[55] EAZY does not use the 24 μm band for the fitting.

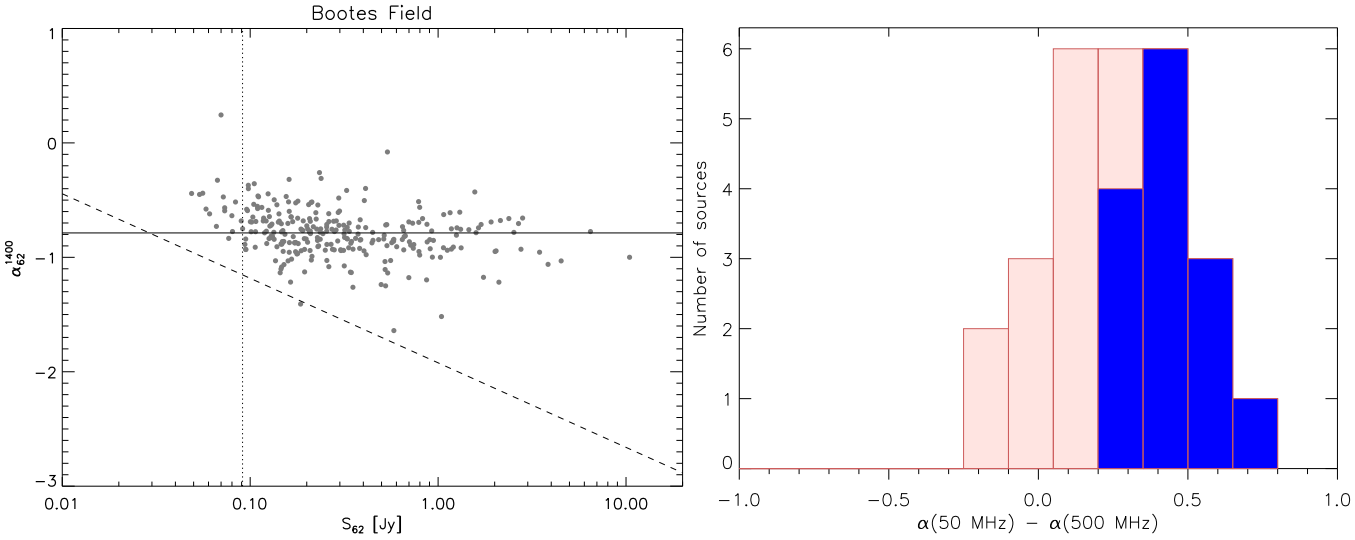

Figure 15. Left: spectral index between 62 and 1400 MHz of sources in the Boötes field plotted against the integrated flux density. The solid line represents the average spectral index of the sources. The vertical dotted line is drawn at $10\sigma_{\rm rms,avg}$, and the dashed line indicates the completeness limit due to the NVSS sensitivity. Right: histogram of spectral curvature between 500 and 50 MHz for bright 34 MHz sources. The spectral curvature was computed by fitting second-order polynomials to the flux density measurements. The blue colors represent sources that cannot be properly fitted with power-law spectra and have $|a_2| > \sigma_{a_2}$; see Section 4.2.

(A color version of this figure is available in the online journal.)

Table 5
USS Sources

Source	R.A., Decl.[a] (J2000)	S_{62} (mJy)	S_{153} (mJy)	S_{1400}[b] (mJy)	α_{62}^{153}	α_{153}^{1400}
J143117.9+351549[c,d]	$14^{\rm h}31^{\rm m}18\overset{\rm s}{.}1$ +35°15′50″	252 ± 41	53 ± 11	1.74 ± 0.08	−1.72 ± 0.29	−1.54 ± 0.10
J143127.4+343506[c,e]	$14^{\rm h}31^{\rm m}27\overset{\rm s}{.}3$ +34°35′07″	140 ± 23	40 ± 8	3.00 ± 0.12	−1.39 ± 0.31	−1.17 ± 0.09
J143236.1+333251[c]	$14^{\rm h}32^{\rm m}36\overset{\rm s}{.}3$ +33°32′54″	65 ± 14	23 ± 5	2.00 ± 0.09	−1.15 ± 0.34	−1.10 ± 0.10
J143345.9+353856[c]	$14^{\rm h}33^{\rm m}46\overset{\rm s}{.}0$ +35°38′55″	153 ± 26	57 ± 12	2.86 ± 0.14[c]	−1.09 ± 0.30	−1.35 ± 0.10
J143501.0+342531[c]	$14^{\rm h}35^{\rm m}01\overset{\rm s}{.}0$ +34°25′31″	173 ± 28	55 ± 11	2.18 ± 0.09	−1.27 ± 0.28	−1.46 ± 0.09
J143426.1+342809[d,f]	$14^{\rm h}34^{\rm m}25\overset{\rm s}{.}6$ +34°28′19″	341 ± 54	115 ± 24	10.1 ± 0.5	−1.20 ± 0.29	−1.10 ± 0.10
J143506.8+350058	$14^{\rm h}35^{\rm m}06\overset{\rm s}{.}9$ +35°00′59″	581 ± 91	141 ± 29	4.02 ± 0.16	−1.57 ± 0.29	−1.61 ± 0.09
J143520.5+345949	$14^{\rm h}35^{\rm m}20\overset{\rm s}{.}5$ +34°59′50″	185 ± 31	57 ± 12	1.55 ± 0.07	−1.30 ± 0.30	−1.63 ± 0.10

Notes.
[a] 1.4 GHz position from de Vries et al. (2002).
[b] 1.4 GHz flux density from de Vries et al. (2002).
[c] Source not detected in the NVSS and/or WENSS survey.
[d] Source detected in the HerMES survey (Roseboom et al. 2010; Oliver et al. 2012; Smith et al. 2012).
[e] Position and flux density from the 1.4 GHz FIRST survey (White et al. 1997).
[f] Position from the 1.4 GHz FIRST survey and flux density from the NVSS survey.

Table 6
USS Sources SED Fit Results

Source	GMRT ID	$P_{\rm match}$ (%)	$N_{\rm bands}$	z_a	$z_{\rm eazy}$ z_m	χ^2/n.d.f.	z	$z_{\rm lrt}$ χ^2/n.d.f.
J143520.5+345949	428	**99.6**	11	0.746	$0.743^{+0.056}_{-0.056}$	1.793	0.70	9.37
J143506.8+350058[a]	440	**86.7**	8	1.988	$2.016^{+0.285}_{-0.279}$	1.054	2.46	1.32
J143506.8+350058	440	13.0	2	...	...	...	...	...
J143501.0+342531	445	**99.4**	11	1.400	$1.380^{+0.171}_{-0.175}$	0.749	1.34	1.91
J143426.1+342809[a]	485	**55.3**	4	...	...	...	...	...
J143426.1+342809[a]	485	41.6	3	...	...	...	...	...
J143345.9+353856	517	**99.8**	6	1.871	$1.935^{+0.125}_{-0.137}$	1.534	2.45	1.93
J143236.1+333251	591	**99.1**	11	0.967	$1.033^{+0.096}_{-0.089}$	1.677	1.06	20.59
J143127.4+343506	667	**76.6**	8	1.815	$1.851^{+0.208}_{-0.182}$	1.549	0.32	0.28
J143127.4+343506[a]	667	23.2	1	...	...	...	...	...
J143117.9+351549	679	**92.4**	7	1.548	$2.253^{+0.750}_{-0.695}$	0.107	1.56	0.09

Notes. The radio source name and GMRT radio source ID are given in Columns 1 and 2; Column 3 gives the probability that a given source is the true optical counterpart to the radio source. The highest probability match is marked in boldface; the number of bands available for SED fitting ($N_{\rm bands}$) is given in Column 4; Columns 5 and 6 give the redshift obtained via EAZY, with z_a the redshift at the minimum χ^2, and z_m the redshift marginalized over the $p(z)$ distribution, with the 68% confidence intervals. The reduced χ^2 of the fit is listed in Column 7; the fitted redshift from the LRT code and corresponding reduced χ^2 are given in Columns 8 and 9.
[a] No SED/$z_{\rm phot}$ fitting could be performed since there are less than five flux measurements were available.

We also selected sources with steep radio spectra ($\alpha < -1.1$) in the Boötes field to find candidate high-z radio galaxies. We identified optical counterparts to these sources and fitted the SEDs to obtain photometric redshifts. We conclude that most of these USS sources seem to be located in the $0.7 \lesssim z \lesssim 2.5$ range.

We thank the anonymous referee for useful comments. LOFAR, the Low Frequency Array designed and constructed by ASTRON, has facilities that are owned by various parties (each with their own funding sources) in several countries, and that are collectively operated by the International LOFAR Telescope (ILT) foundation under a joint scientific policy. This work made use of images and/or data products provided by the NOAO Deep Wide-Field Survey (Jannuzi & Dey 1999), which is supported by the National Optical Astronomy Observatory (NOAO). NOAO is operated by AURA, Inc., under a cooperative agreement with the National Science Foundation.

Support for this work was provided by NASA through Einstein Postdoctoral grant Number PF2-130104 awarded by the *Chandra* X-ray Center, which is operated by the Smithsonian Astrophysical Observatory for NASA under contract NAS8-03060. Chiara Ferrari acknowledges financial support by the "*Agence Nationale de la Recherche*" through grant ANR-09-JCJC-0001-01.

APPENDIX A

EXTENDED SOURCES AT 62 MHz

Figures 16 and 17 show the 62 MHz LOFAR images of extended sources in the Boötes and 3C 295 fields.

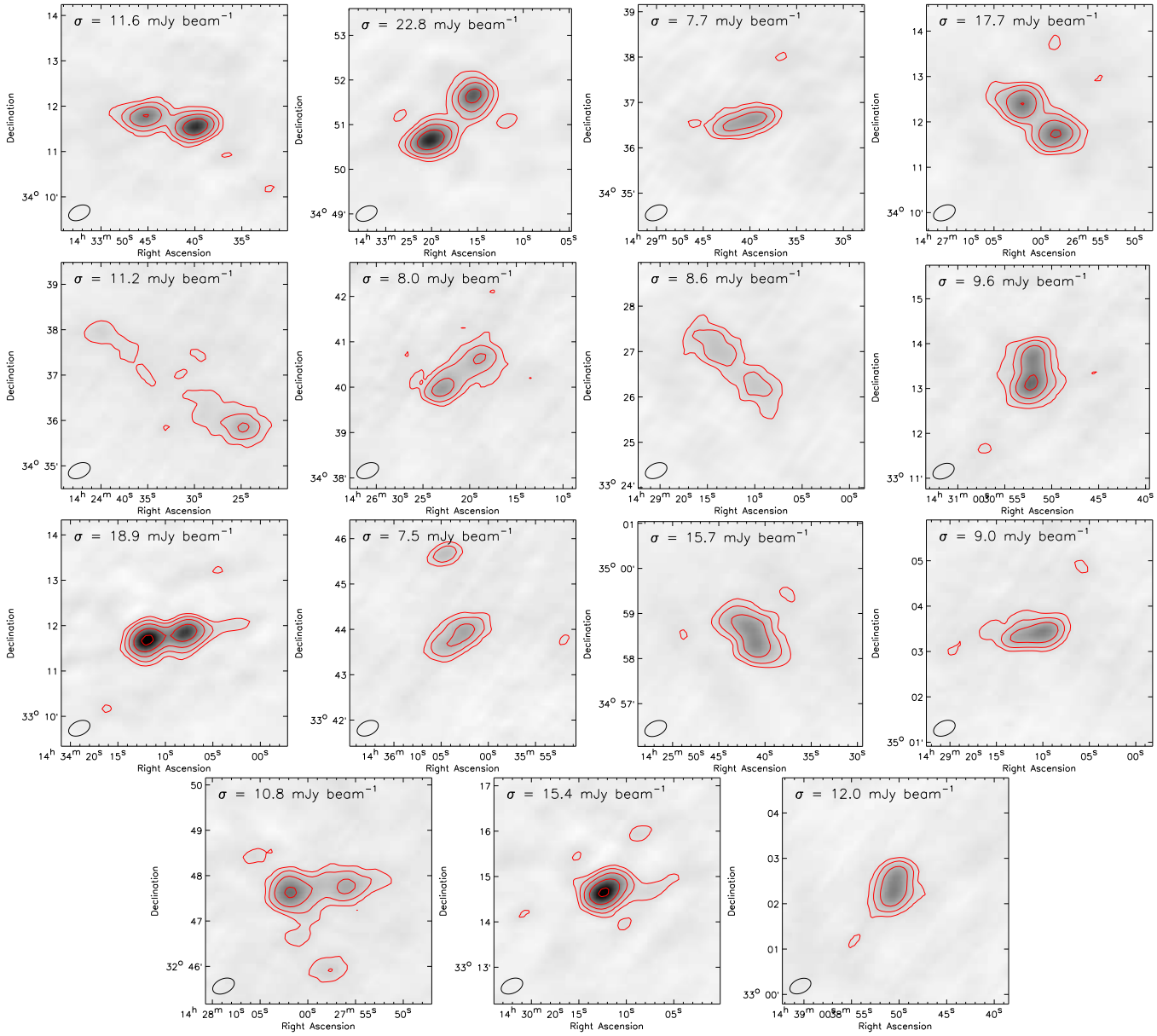

Figure 16. Images of resolved sources in the Boötes field at 62 MHz. Contour levels are drawn at [1, 2, 4, 8, ...] × $3\sigma_{\text{local rms}}$, with $\sigma_{\text{local rms}}$ reported in each image. The beam size is shown in the bottom left corner of the images.

(A color version of this figure is available in the online journal.)

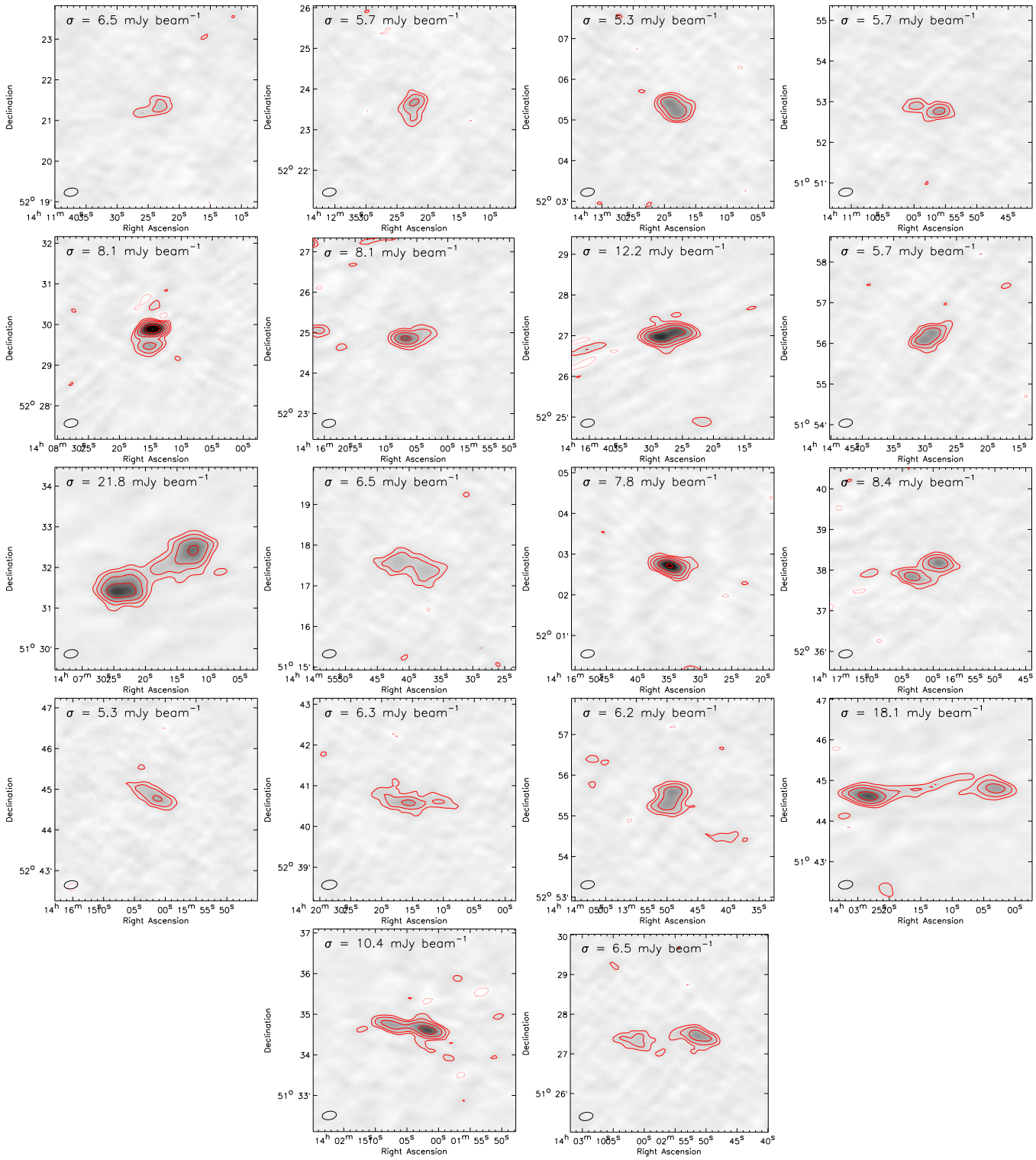

Figure 17. Images of resolved sources in the 3C 295 field at 62 MHz. Contour levels are drawn at $[1, 2, 4, 8, \ldots] \times 3\sigma_{\rm local\ rms}$, with $\sigma_{\rm local\ rms}$ reported in each image. The beam size is shown in the bottom left corner of the images.

(A color version of this figure is available in the online journal.)

APPENDIX B

SED AND PHOTO-z FITTING RESULTS

Figure 18 shows the SEDs for each counterpart to a USS source and I band, IRAC 4.5 μm, IRAC 8.0 μm, and MIPS 24 μm postage stamps, with GMRT (and FIRST where there is a source) contours overlaid.

APPENDIX C

SOURCE COUNTS AT 62 MHz FOR THE BOÖTES FIELD AND 3C 295 FIELDS

Figure 19 shows the separate Euclidean-normalized differential source counts at 62 MHz for the Boötes and 3C 295 fields. The combined source counts are shown in Figure 13.

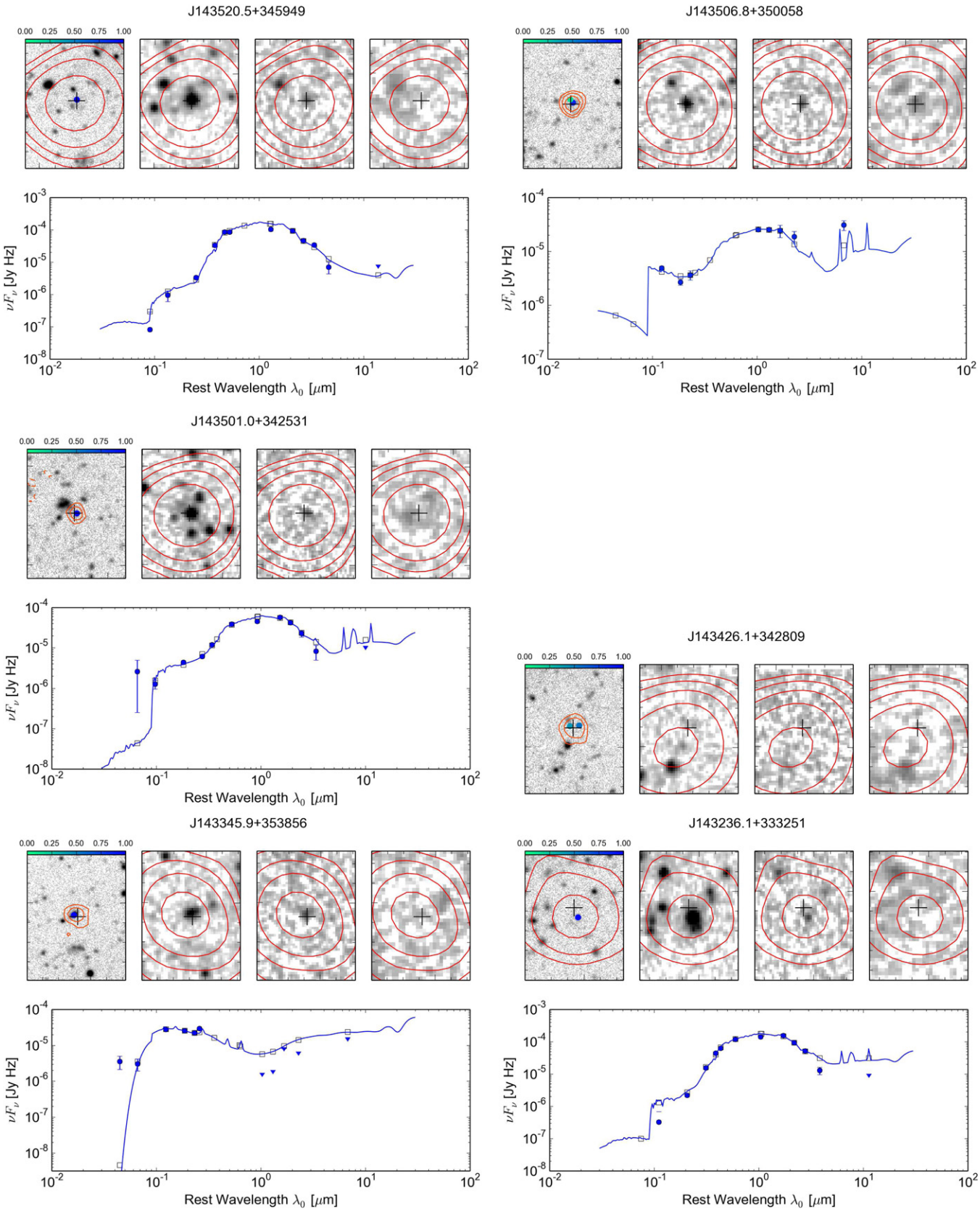

Figure 18. Top panels: postage stamps showing NDWFS *I*-band, IRAC 4.5 μm, IRAC 8.0 μm, and MIPS 24 μm images. GMRT 153 MHz (red) and FIRST 1.4 GHz (orange, when available) contours are overlaid. Radio contour levels are drawn at $[1, 2, 4, \ldots] \times 3\sigma_{\rm rms}$. A black cross indicates the GMRT radio position and the color scale at the top of the *I*-band image shows the probability that the *I*-band source, marked with a colored point, is the true optical counterpart. Bottom panels: spectral energy distribution and best fitted LRT model for the optical counterpart(s). The flux measurements were taken from Jannuzi & Dey (1999), Elston et al. (2006), Cool (2007), Ashby et al. (2009), Morrissey et al. (2007), and Jannuzi et al. (2010).

(A color version of this figure is available in the online journal.)

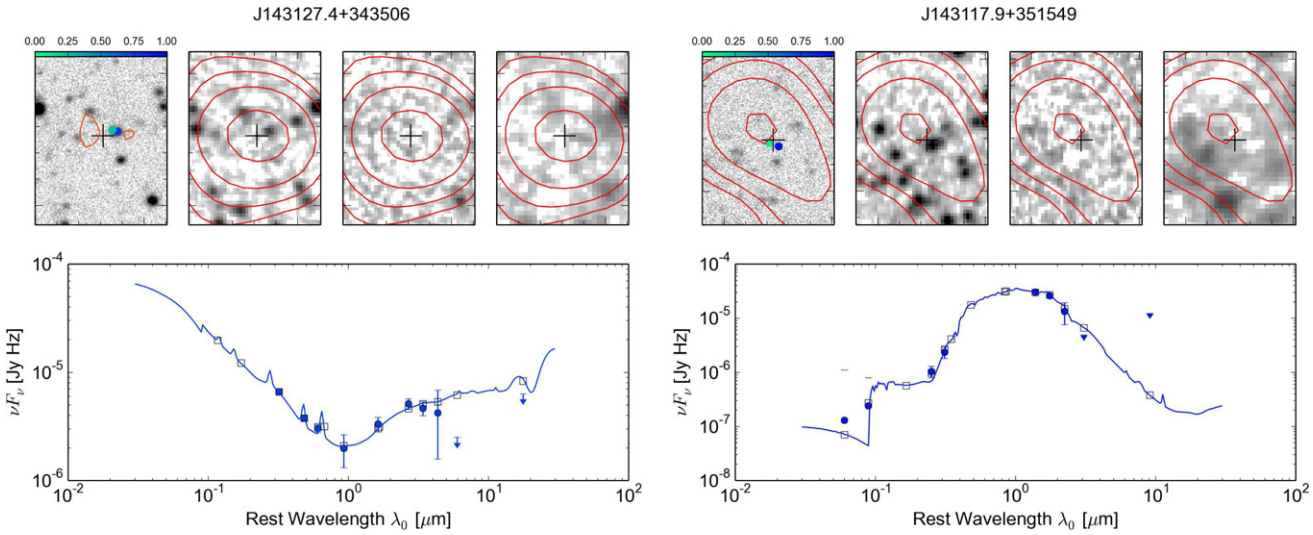

Figure 18. (Continued)

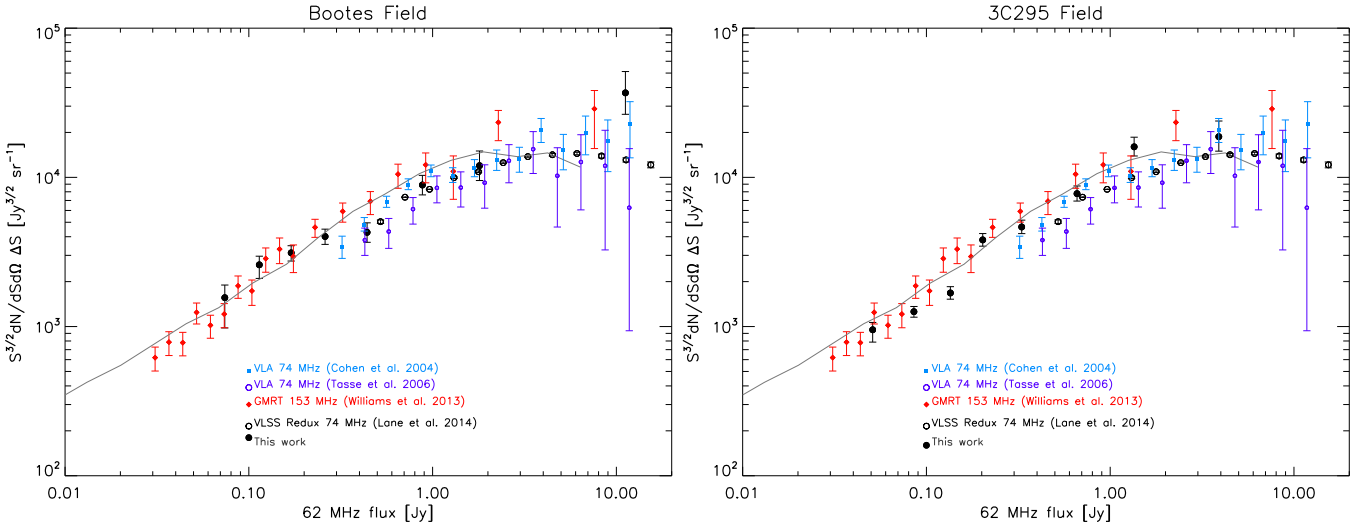

Figure 19. Euclidean-normalized differential source counts at 62 MHz for the Boötes and 3C 295 fields. The LOFAR points are indicated by the black symbols. Red diamonds are Boötes field source counts at 153 MHz, scaled to 62 MHz using $\alpha = -0.7$. Black open circles, blue squares, and purple open circles are 74 MHz differential source counts from Tasse et al. (2006), Cohen et al. (2004), and Lane et al. (2014), and the solid gray line displays the counts from the 151 MHz SKADS S^3-SEX simulation (Wilman et al. 2008). These are all scaled to 62 MHz assuming $\alpha = -0.7$.

(A color version of this figure is available in the online journal.)

REFERENCES

Ashby, M. L. N., Stern, D., Brodwin, M., et al. 2009, ApJ, 701, 428
Assef, R. J., Kochanek, C. S., Brodwin, M., et al. 2008, ApJ, 676, 286
Bhatnagar, S., Cornwell, T. J., Golap, K., & Uson, J. M. 2008, A&A, 487, 419
Brammer, G. B., van Dokkum, P. G., & Coppi, P. 2008, ApJ, 686, 1503
Briggs, D. S. 1995, PhD thesis, New Mexico Institute of Mining Technology
Brookes, M. H., Best, P. N., Rengelink, R., & Röttgering, H. J. A. 2006, MNRAS, 366, 1265
Cohen, A. S., Lane, W. M., Cotton, W. D., et al. 2007, AJ, 134, 1245
Cohen, A. S., Röttgering, H. J. A., Jarvis, M. J., Kassim, N. E., & Lazio, T. J. W. 2004, ApJS, 150, 417
Cohen, A. S., Röttgering, H. J. A., Kassim, N. E., et al. 2003, ApJ, 591, 640
Condon, J. J., Cotton, W. D., Greisen, E. W., et al. 1998, AJ, 115, 1693
Cool, R. J. 2007, ApJS, 169, 21
Cotton, W. D., & Uson, J. M. 2008, A&A, 490, 455
Croft, S., Bower, G. C., & Whysong, D. 2013, ApJ, 762, 93
Croft, S., van Breugel, W., Brown, M. J. I., et al. 2008, AJ, 135, 1793
Cruz, M. J., Jarvis, M. J., Rawlings, S., & Blundell, K. M. 2007, MNRAS, 375, 1349
De Breuck, C., van Breugel, W., Röttgering, H. J. A., & Miley, G. 2000, A&AS, 143, 303
de Gasperin, F., Intema, H. T., Williams, W., et al. 2014, MNRAS, 440, 1542
Delain, K. M., & Rudnick, L. 2006, AN, 327, 561
de Vries, W. H., Morganti, R., Röttgering, H. J. A., et al. 2002, AJ, 123, 1784
Elston, R. J., Gonzalez, A. H., McKenzie, E., et al. 2006, ApJ, 639, 816
Hales, S. E. G., Waldram, E. M., Rees, N., & Warner, P. J. 1995, MNRAS, 274, 447
Hamaker, J. P. 2011, Mathematical-physical Analysis of the Generic Dual-dipole Antenna, Tech. Rep. (Dwingeloo, The Netherlands: ASTRON)
Hamaker, J. P., & Bregman, J. D. 1996, A&AS, 117, 161
Heald, G., McKean, J., Pizzo, R., et al. 2010, in ISKAF2010 Science Meeting (Trieste, Italy: Proc. of Science)
Heywood, I., Jarvis, M. J., & Condon, J. J. 2013, MNRAS, 432, 2625
Higdon, J. L., Higdon, S. J. U., Weedman, D. W., et al. 2005, ApJ, 626, 58
Intema, H. T., van Weeren, R. J., Röttgering, H. J. A., & Lal, D. V. 2011, A&A, 535, A38
Ishwara-Chandra, C. H., & Marathe, R. 2007, in ASP Conf. Ser. 380, Deepest Astronomical Surveys, ed. J. Afonso, H. C. Ferguson, B. Mobasher, & R. Norris (San Francisco, CA: ASP), 237
Ishwara-Chandra, C. H., Sirothia, S. K., Wadadekar, Y., Pal, S., & Windhorst, R. 2010, MNRAS, 405, 436
Ivison, R. J., Chapman, S. C., Faber, S. M., et al. 2007, ApJL, 660, L77
Jannuzi, B., Weiner, B., Block, M., et al. 2010, BAAS, 42, 215

Jannuzi, B. T., & Dey, A. 1999, in ASP Conf. Ser. 191, Photometric Redshifts and the Detection of High Redshift Galaxies, ed. R. Weymann, L. Storrie-Lombardi, M. Sawicki, & R. Brunner (San Francisco, CA: ASP), 111
Jarvis, M. J., Rawlings, S., Lacy, M., et al. 2001, MNRAS, 326, 1563
Jarvis, M. J., Teimourian, H., Simpson, C., et al. 2009, MNRAS, 398, L83
Kassim, N. E., Lazio, T. J. W., Erickson, W. C., et al. 2007, ApJS, 172, 686
Ker, L. M., Best, P. N., Rigby, E. E., Röttgering, H. J. A., & Gendre, M. A. 2012, MNRAS, 420, 2644
Kunert-Bajraszewska, M., Gawroński, M. P., Labiano, A., & Siemiginowska, A. 2010, MNRAS, 408, 2261
Lacy, M., Rawlings, S., & Warner, P. J. 1992, MNRAS, 256, 404
Lane, W. M., Cotton, W. D., Helmboldt, J. F., & Kassim, N. E. 2012, RaSc, 47, RS0K04
Lane, W. M., Cotton, W. D., van Velzen, S., et al. 2014, MNRAS, 440, 327
Miley, G., & De Breuck, C. 2008, A&ARv, 15, 67
Morrissey, P., Conrow, T., Barlow, T. A., et al. 2007, ApJS, 173, 682
Murgia, M., Parma, P., Mack, K.-H., et al. 2011, A&A, 526, A148
Offringa, A. R., de Bruyn, A. G., Biehl, M., et al. 2010, MNRAS, 405, 155
Offringa, A. R., de Bruyn, A. G., Zaroubi, S., et al. 2013, A&A, 549, A11
Offringa, A. R., van de Gronde, J. J., & Roerdink, J. B. T. M. 2012, A&A, 539, A95
Oliver, S. J., Bock, J., Altieri, B., et al. 2012, MNRAS, 424, 1614
Pandey, V. N., van Zwieten, J. E., de Bruyn, A. G., & Nijboer, R. 2009, in ASP Conf. Ser. 407, The Low-Frequency Radio Universe, ed. D. J. Saikia, D. A. Green, Y. Gupta, & T. Venturi (San Francisco, CA: ASP), 384
Parma, P., Murgia, M., de Ruiter, H. R., et al. 2007, A&A, 470, 875
Perley, R. A., & Taylor, G. B. 1991, AJ, 101, 1623
Rau, U., & Cornwell, T. J. 2011, A&A, 532, A71
Rees, N. 1990, MNRAS, 244, 233
Rengelink, R. B., Tang, Y., de Bruyn, A. G., et al. 1997, A&AS, 124, 259
Roseboom, I. G., Oliver, S. J., Kunz, M., et al. 2010, MNRAS, 409, 48
Scaife, A. M. M., & Heald, G. H. 2012, MNRAS, 423, L30
Sirothia, S. K., Saikia, D. J., Ishwara-Chandra, C. H., & Kantharia, N. G. 2009, MNRAS, 392, 1403
Smirnov, O. M. 2011, A&A, 527, A107
Smith, A. J., Wang, L., Oliver, S. J., et al. 2012, MNRAS, 419, 377
Sutherland, W., & Saunders, W. 1992, MNRAS, 259, 413
Tasse, C., Cohen, A. S., Röttgering, H. J. A., et al. 2006, A&A, 456, 791
Tasse, C., Le Borgne, D., Röttgering, H., et al. 2008, A&A, 490, 879
Tasse, C., van der Tol, S., van Zwieten, J., van Diepen, G., & Bhatnagar, S. 2013, A&A, 553, A105
van der Tol, S., Jeffs, B. D., & van der Veen, A.-J. 2007, ITSP, 55, 4497
van Haarlem, M. P., Wise, M. W., Gunst, A. W., et al. 2013, A&A, 556, A2
van Weeren, R. J., Röttgering, H. J. A., Brüggen, M., & Cohen, A. 2009, A&A, 508, 75
van Weeren, R. J., Röttgering, H. J. A., Rafferty, D. A., et al. 2012, A&A, 543, A43
White, R. L., Becker, R. H., Helfand, D. J., & Gregg, M. D. 1997, ApJ, 475, 479
Williams, W. L., Intema, H. T., & Röttgering, H. J. A. 2013, A&A, 549, A55
Wilman, R. J., Miller, L., Jarvis, M. J., et al. 2008, MNRAS, 388, 1335
Windhorst, R. A., Miley, G. K., Owen, F. N., Kron, R. G., & Koo, D. C. 1985, ApJ, 289, 494